

A HIGH-ORDER FINITE DIFFERENCE WENO SCHEME FOR IDEAL MAGNETOHYDRODYNAMICS ON CURVILINEAR MESHES

ANDREW J. CHRISTLIEB*, XIAO FENG[†], YAN JIANG[‡], AND QI TANG[§]

Abstract. A high-order finite difference numerical scheme is developed for the ideal magnetohydrodynamic equations based on an alternative flux formulation of the weighted essentially non-oscillatory (WENO) scheme. It computes a high-order numerical flux by a Taylor expansion in space, with the lowest-order term solved from a Riemann solver and the higher-order terms constructed from physical fluxes by limited central differences. The scheme coupled with several Riemann solvers, including a Lax-Friedrichs solver and HLL-type solvers, is developed on general curvilinear meshes in two dimensions and verified on a number of benchmark problems. In particular, a HLLD solver on Cartesian meshes is extended to curvilinear meshes with proper modifications. A numerical boundary condition for the perfect electrical conductor (PEC) boundary is derived for general geometry and verified through a bow shock flow. Numerical results also confirm the advantages of using low dissipative Riemann solvers in the current framework.

Key word. WENO; finite difference methods; curvilinear meshes; magnetohydrodynamics; constrained transport

1. Introduction. The ideal magnetohydrodynamic (MHD) equations are a fluid model to describe the dynamics of a perfectly conducting quasi-neutral plasma. The equations are a system of nonlinear hyperbolic conservation laws with the constraint that its magnetic field is divergence free. In this work, we describe a high-order finite difference schemes for ideal MHD based on an alternative flux formulation of the weighted essentially non-oscillatory (WENO) scheme [41, 42, 54]. The resultant scheme is applicable to general curvilinear meshes, which can be obtained by a smooth or non-smooth mapping, and compatible with many approximate Riemann solvers.

In recent years, high-order numerical schemes using essentially non-oscillatory (ENO) and WENO approaches have been extended to the ideal MHD equations in [2, 5, 14, 17, 36, 40, 45, 52, 55] for example. Many of those ENO/WENO approaches use the idea of *reconstruction*, in which a numerical flux is typically reconstructed from the physical flux. We refer the reader to the review paper [53] for details. However, the results in [48, 60] show that when a standard finite difference WENO scheme is applied to curvilinear meshes, the free-stream preservation condition is not satisfied, which will cause large errors and even lead to numerical instabilities for high-order schemes. This issue can be resolved by an alternative flux formulation for the conservative finite difference WENO scheme in [54]. In this formulation, a WENO interpolation procedure is applied to the solution rather than to the flux functions. In [42], it has been theoretically proved and numerically demonstrated that this scheme can preserve free-stream solutions on both stationary and dynamically generalized coordinate systems, hence giving much better performance than the standard finite difference WENO schemes on curvilinear meshes. In addition, the alternative flux formulation takes advantage of monotone fluxes for the scalar case and approximate Riemann solvers for the system case, while the standard finite difference WENO schemes can only use certain fluxes since its nonlinear stability relies on a smooth flux splitting. Note that the most commonly used flux splitting in finite difference schemes is a Lax-Friedrichs flux splitting, which is one of the most diffusive Riemann solvers. Therefore, in this work we rely on the alternative flux formulation of the WENO schemes to solve the MHD equations on curvilinear meshes.

The alternative flux formulation requires an approximated Riemann solver in the low-order terms. In this work, a Lax-Friedrichs Riemann solver and HLL-type Riemann solvers are used. The HLL Riemann solver, first proposed in [30], solves a Riemann problem by an approximate solution consisting of one intermediate state that is connected to the left and right states by discontinuities. This intermediate state is obtained by exploiting the conservation of the equations, commonly referred to as the *consistency condition*. When applied to the Euler equations in hydrodynamics, the HLL solver exhibits excessive dissipations in the presence of contact discontinuities. To remedy this, a HLLC (C stands for contact) solver is proposed for

*Department of Computational Mathematics, Science and Engineering, Department of Mathematics and Department of Electrical and Computer Engineering, Michigan State University, East Lansing, MI (christli@msu.edu). Research is supported in part by AFOSR grants FA9550-12-1-0343, FA9550-12-1-0455, FA9550-15-1-0282 and NSF grant DMS-1418804.

[†]The MathWorks, Inc., Natick, MA (xiao.feng@mathworks.com).

[‡]Department of Mathematics, Michigan State University, East Lansing, MI (jiangyan@math.msu.edu).

[§]Department of Mathematical Sciences, Rensselaer Polytechnic Institute, Troy, NY (tangq3@rpi.edu). Research is supported by the Eliza Ricketts Postdoctoral Fellowship.

the Euler equations in [58]. It assumes two intermediate states in the approximate solution, which are connected to each other by a contact discontinuity and connected to the left and right states by shocks. The *Rankine-Hugoniot condition*, in addition to the consistency condition, is used to determine the intermediate states. Similar ideas were later used in designing Riemann solvers for the ideal MHD equations in [29, 44, 46]. The solvers in [29, 44] were both named HLLC solvers for ideal MHD, because two intermediate states are assumed to be connected to each other by a contact discontinuity. The solver in [46] was named HLLD (D stands for discontinuities) solver for ideal MHD, since the solver involving four intermediate states can exactly resolve most types of discontinuities, the only exception being the slow shocks. Note that the HLL and HLLC solvers can be directly applied to general curvilinear meshes while the HLLD solver is previously designed for Cartesian meshes. Besides the aforementioned one-dimensional Riemann solvers, we note that there are recent developments of multidimensional Riemann solvers for ideal MHD, see [3, 4, 6] for instance. In the current work, we experiment the HLL-type solvers when exploring the effects of the choice of Riemann solver in the current framework. In particular, the HLLD solver is extended to curvilinear meshes.

One of the main numerical difficulties for simulating the ideal MHD equations is to control divergence errors in the magnetic field. Failure to control the divergence error creates an unphysical force parallel to the magnetic field (see [10] for instance), which may eventually result into numerical instabilities as its effects accumulate. There are mainly four types of numerical approaches to address this issue, including (1) the non-conservative eight-wave method [28], (2) the projection method [10], (3) the hyperbolic divergence cleaning method [22], and (4) the various constrained transport methods [1, 8, 17, 18, 24, 25, 31, 32, 50]. See the review paper [59] for more discussions on the advantages and disadvantages of those approaches. In this work, we use a finite difference constrained transport method proposed in [17] to address this issue.

The main motivation for using curvilinear meshes in the current work is that in certain MHD applications, the complex geometry is easier to describe using boundary-fitted grids in a curvilinear coordinate system, see [12, 23, 27, 36, 49] for instance. In a curvilinear coordinate, it is also relatively easier for finite difference methods to impose boundary conditions in the presence of curved surfaces, compared to some other approaches such as cut-cell methods. In this work, we impose several boundary conditions in the numerical tests for the ideal MHD equations, including the inflow and outflow boundary conditions, and a perfect electrical conductor (PEC) condition. In particular, we derive a numerical compatibility boundary condition for the PEC boundary for the both conserved quantities and magnetic potential, based on the previous work in the Euler equations [34] and Maxwell's equations [33]. Some discussions of the numerical boundary conditions for the ideal MHD equations can be found in [35, 55], in which the PEC boundary is implemented differently through a least-squares reconstruction to set the normal components of the velocity and magnetic field to zero. Instead, we rely on the governing equations and a local characteristic analysis to derive the numerical boundary condition.

The remaining sections of the paper are organized as follows. The governing equations are reviewed in Section 2. The details of the alternative flux formulation are presented in Section 3, including an outline of the base scheme, an additional limiter applied to higher order terms and its extensions to ideal MHD and curvilinear meshes. Section 4 presents some numerical approaches applied to the ideal MHD simulations, which include a brief outline of the constrained transport method and a positivity-preserving limiter, and a derivation of numerical boundary conditions for the PEC boundary. Numerical results are presented in Section 5. Conclusions and future directions are given in Section 6. A WENO interpolation is described in Appendix A. Several HLL-type Riemann solvers are detailed in Appendix B, including our version of the HLLD solver.

2. Governing equations. In this section we briefly review the ideal MHD equations, with an emphasis on the hyperbolicity and discontinuities of the system. In a conservation form, the ideal MHD equations are

$$(1) \quad \partial_t \begin{bmatrix} \rho \\ \rho \mathbf{u} \\ \mathcal{E} \\ \mathbf{B} \end{bmatrix} + \nabla \cdot \begin{bmatrix} \rho \mathbf{u} \\ \rho \mathbf{u} \otimes \mathbf{u} + p_{\text{tot}} \mathbb{I} - \mathbf{B} \otimes \mathbf{B} \\ \mathbf{u}(\mathcal{E} + p_{\text{tot}}) - \mathbf{B}(\mathbf{u} \cdot \mathbf{B}) \\ \mathbf{u} \otimes \mathbf{B} - \mathbf{B} \otimes \mathbf{u} \end{bmatrix} = 0,$$

$$(2) \quad \nabla \cdot \mathbf{B} = 0,$$

where ρ is the mass density, $\rho \mathbf{u} = (\rho u, \rho v, \rho w)^T$ is the momentum density, \mathcal{E} is the total energy density, $\mathbf{B} = (B_1, B_2, B_3)^T$ is the magnetic field, p is the thermal pressure, $\|\cdot\|$ is the Euclidean vector norm, and

$p_{\text{tot}} = p + \frac{1}{2}\|\mathbf{B}\|^2$ is the total pressure. Let $\gamma = 5/3$ be the ideal gas constant, and the pressure satisfies the equation of state

$$\mathcal{E} = \frac{p}{\gamma - 1} + \frac{\rho \|\mathbf{u}\|^2}{2} + \frac{\|\mathbf{B}\|^2}{2}.$$

2.1. Waves in the ideal MHD equations. The wave speeds of the ideal MHD system (1) in some arbitrary direction \mathbf{n} ($\|\mathbf{n}\| = 1$) are

$$\begin{aligned} (3a) \quad & \lambda_{1,8} = \mathbf{u} \cdot \mathbf{n} \mp c_f && \text{(fast magnetosonic waves),} \\ (3b) \quad & \lambda_{2,7} = \mathbf{u} \cdot \mathbf{n} \mp c_a && \text{(Alfvén waves),} \\ (3c) \quad & \lambda_{3,6} = \mathbf{u} \cdot \mathbf{n} \mp c_s && \text{(slow magnetosonic waves),} \\ (3d) \quad & \lambda_4 = \lambda_5 = \mathbf{u} \cdot \mathbf{n} && \text{(entropy and divergence waves),} \end{aligned}$$

where

$$\begin{aligned} a &= \sqrt{\frac{\gamma p}{\rho}} && \text{(sound speed),} \\ c_a &= \sqrt{\frac{(\mathbf{B} \cdot \mathbf{n})^2}{\rho}} && \text{(Alfvén speed),} \\ c_f &= \left[\frac{1}{2} \left(a^2 + \frac{\|\mathbf{B}\|^2}{\rho} + \sqrt{\left(a^2 + \frac{\|\mathbf{B}\|^2}{\rho} \right)^2 - 4a^2 \frac{(\mathbf{B} \cdot \mathbf{n})^2}{\rho}} \right) \right]^{\frac{1}{2}} && \text{(fast magnetosonic speed),} \\ c_s &= \left[\frac{1}{2} \left(a^2 + \frac{\|\mathbf{B}\|^2}{\rho} - \sqrt{\left(a^2 + \frac{\|\mathbf{B}\|^2}{\rho} \right)^2 - 4a^2 \frac{(\mathbf{B} \cdot \mathbf{n})^2}{\rho}} \right) \right]^{\frac{1}{2}} && \text{(slow magnetosonic speed).} \end{aligned}$$

The eigen-decomposition of the Jacobian matrix for ideal MHD equations is complicated and has its own subtleties, see [9] for instance. More details of MHD waves can be found in many MHD literature, see [37, 9] for example.

2.2. Discontinuities in the ideal MHD equations. The different types of discontinuities in the ideal MHD equations (1) are reviewed in this section. Those discontinuities are used in the later discussion of the Riemann solvers in Appendix B. Let $\mathbf{q}(t, \mathbf{x})$ denote the conserved quantities of the system, and assume the Riemann problem has an initial condition given by

$$(4) \quad \mathbf{q}(0, \mathbf{x}) = \begin{cases} \mathbf{q}_L, & \text{if } \mathbf{n} \cdot \mathbf{x} < 0, \\ \mathbf{q}_R, & \text{if } \mathbf{n} \cdot \mathbf{x} \geq 0, \end{cases}$$

where \mathbf{q}_L and \mathbf{q}_R are constant vectors, and \mathbf{n} is an arbitrary direction. The solution to such a problem is a function \mathbf{q} that depends only on t and $\mathbf{n} \cdot \mathbf{x}$. We are interested in the case when the solution consists of a single moving discontinuity given by

$$(5) \quad \mathbf{q}(t, \mathbf{x}) = \begin{cases} \mathbf{q}_L, & \text{if } (\mathbf{n} \cdot \mathbf{x})/t < S, \\ \mathbf{q}_R, & \text{if } (\mathbf{n} \cdot \mathbf{x})/t \geq S, \end{cases}$$

where S is the speed at which the discontinuity moves. Let \mathbf{F} denote the flux in the direction \mathbf{n} . The *Rankine-Hugoniot (RH) condition* of the hyperbolic conservation law is

$$(6) \quad S(\mathbf{q}_R - \mathbf{q}_L) = \mathbf{F}(\mathbf{q}_R) - \mathbf{F}(\mathbf{q}_L).$$

Note that the divergence condition (2) in the ideal MHD equations implies that the magnetic field in the initial conditions (4) satisfy

$$(7) \quad \mathbf{n} \cdot \mathbf{B}_L = \mathbf{n} \cdot \mathbf{B}_R.$$

The RH condition (6) and the constraint (7) imply that a single moving discontinuity in ideal MHD must be one from the following list:

1. A (fast or slow) *shock*. In this case, the solutions satisfy

$$\begin{aligned}\mathbf{n} \cdot \mathbf{u}_\alpha &\neq S, & \alpha = L, R, \\ \mathbf{n} \cdot \mathbf{u}_L &\neq \mathbf{n} \cdot \mathbf{u}_R, \\ \rho_L &\neq \rho_R.\end{aligned}$$

2. A *rotational discontinuity*. In this case, the solutions satisfy

$$\begin{aligned}\mathbf{n} \cdot \mathbf{u}_\alpha &\neq S, & \alpha = L, R, \\ \mathbf{n} \cdot \mathbf{u}_L &= \mathbf{n} \cdot \mathbf{u}_R, \\ \rho_L &= \rho_R, \\ \mathbf{t}_i \cdot (\mathbf{u}_R - \mathbf{u}_L) &= \frac{1}{\sqrt{\rho}} \mathbf{t}_i \cdot (\mathbf{B}_R - \mathbf{B}_L), & i = 1, 2,\end{aligned}$$

where \mathbf{t}_1 and \mathbf{t}_2 are the tangential vectors with respect to the discontinuity interface.

3. A *contact discontinuity*. In this case, the solutions satisfy

$$\begin{aligned}\mathbf{n} \cdot \mathbf{B}_\alpha &\neq 0, & \alpha = L, R, \\ \mathbf{B}_L &= \mathbf{B}_R, \\ \mathbf{u}_L &= \mathbf{u}_R, \\ p_L &= p_R.\end{aligned}$$

4. A *tangential discontinuity*. In this case, the solutions satisfy

$$\begin{aligned}\mathbf{n} \cdot \mathbf{B}_\alpha &= 0, & \alpha = L, R, \\ p_{\text{tot}L} &= p_{\text{tot}R}.\end{aligned}$$

Here the jumps in the tangential velocities and tangential magnetic fields can be arbitrary.

Note that shocks are the only types of discontinuities that can possibly admit jumps in the normal velocities or the total pressures. Rotational, contact, and tangential discontinuities are *linearly degenerate*. Rotational discontinuities correspond to Alfvén waves, while contact and tangential discontinuities correspond to entropy and divergence waves. None of the discontinuities in this list is genuinely nonlinear. The discussions on discontinuities in the ideal MHD equations can be also found in [56].

The divergence-free condition suggests $\mathbf{n} \cdot \mathbf{B}$ must be identical on both sides of the discontinuity. However, this relation does not hold in multiple dimensions in numerical simulations. Therefore, Riemann solvers need special treatments for such cases. The treatment in our version of the HLLD solver will be discussed in Appendix B.

3. An alternative flux formulation of the WENO scheme. In this section, we describe a WENO scheme based on an alternative flux formulation from [41, 42, 54]. The basic scheme is first given for a system of conservation laws. Numerical experiments indicate that its direct extension to the MHD equations causes oscillations in some benchmark problems. Hence, a limiter is introduced in Section 3.2 to control those oscillations. The extensions of the base scheme to curvilinear coordinates are given in Sections 3.3.

3.1. Basic scheme. A one-dimensional system of conservation law takes the form

$$(8) \quad \partial_t \mathbf{q} + \partial_x \mathbf{f}(\mathbf{q}) = 0,$$

where the conserved variables $\mathbf{q} = (q_1(t, x), \dots, q_n(t, x))^T$ is a vector function of t and x and $\mathbf{f}(\mathbf{q}) = (f_1(\mathbf{q}), \dots, f_n(\mathbf{q}))^T$ is a flux function. A hyperbolic system (8) indicates the Jacobian $\partial \mathbf{f} / \partial \mathbf{q}$ has n real eigenvalues satisfying $\lambda_1(\mathbf{q}) \leq \dots \leq \lambda_n(\mathbf{q})$ and a set of n independent (right) eigenvectors, $\{\mathbf{r}_1(\mathbf{q}), \dots, \mathbf{r}_n(\mathbf{q})\}$. Defining a matrix

$$R(\mathbf{q}) = (\mathbf{r}_1(\mathbf{q}), \dots, \mathbf{r}_n(\mathbf{q})),$$

we note that the Jacobian matrix satisfies

$$R^{-1}(\mathbf{q}) \frac{\partial \mathbf{f}}{\partial \mathbf{q}} R(\mathbf{q}) = \text{diag}(\lambda_1(\mathbf{q}), \dots, \lambda_n(\mathbf{q})).$$

The system (8) is solved by a semi-discrete conservative finite difference scheme of the form

$$(9) \quad \partial_t \mathbf{q}_i + \frac{1}{\Delta x} (\hat{\mathbf{f}}_{i+1/2} - \hat{\mathbf{f}}_{i-1/2}) = 0,$$

on a uniform mesh with $x_i = i\Delta x$. Here $\mathbf{q}_i(t)$ sits on x_i , which is the numerical approximation to the point value $\mathbf{q}(x_i, t)$, and $\hat{\mathbf{f}}$ is some numerical flux that sits on half grid points. Note that $\hat{\mathbf{f}}$ is a vector function and the k -th component of the numerical flux satisfies

$$(10) \quad \frac{1}{\Delta x} (\hat{f}_k|_{i+1/2} - \hat{f}_k|_{i-1/2}) = \partial_x f_k(\mathbf{q}(x))|_{x=x_i} + \mathcal{O}(\Delta x^m),$$

where m is the spatial order of accuracy of the scheme. The semi-discrete form (9) is then integrated in time using a time-stepping method, such as Runge-Kutta (RK) methods. In the current work, a third-order TVD-RK method is used.

The alternative flux formulation of the WENO scheme $\hat{\mathbf{f}}$ at $x_{i+1/2}$, first proposed in [54], is given by

$$(11) \quad \hat{\mathbf{f}}_{i+1/2} = \mathbf{f}_{i+1/2} + \sum_{k=1}^{[(m-1)/2]} a_{2k} \Delta x^{2k} \partial_x^{2k} \mathbf{f}|_{i+1/2}$$

to guarantee m -th order accuracy in (10), where a_{2k} 's are some constants obtained by Taylor expansions and the accuracy constraint. In the current work, a truncation at $m = 5$ is used and $\hat{\mathbf{f}}$ is therefore approximated by

$$(12) \quad \hat{\mathbf{f}}_{i+1/2} = \mathbf{f}_{i+1/2} - \frac{1}{24} \Delta x^2 \partial_x^2 \mathbf{f}|_{i+1/2} + \frac{7}{5760} \Delta x^4 \partial_x^4 \mathbf{f}|_{i+1/2}.$$

The first term in (12) is approximated by

$$(13) \quad \mathbf{f}_{i+1/2} = \mathbf{F}(\mathbf{q}_{i+1/2}^-, \mathbf{q}_{i+1/2}^+),$$

where \mathbf{F} is a Riemann solver and $\mathbf{q}_{i+1/2}^\pm$ are sufficiently high-order one-sided approximations to \mathbf{q} at $x_{i+1/2}$. The WENO interpolation is used to obtain $\mathbf{q}_{i+1/2}^\pm$, and the formulation of a fifth-order WENO interpolation is given in Appendix A. Approximate Riemann solvers are used in the current work, including a Lax-Friedrich solver and HLL-type Riemann solvers. For instance, a Lax-Friedrichs solver gives

$$(14) \quad \mathbf{F}(\mathbf{q}^-, \mathbf{q}^+) = \frac{1}{2} [\mathbf{f}(\mathbf{q}^-) + \mathbf{f}(\mathbf{q}^+) - \alpha (\mathbf{q}^+ - \mathbf{q}^-)],$$

with $\alpha = \max_{1 \leq k \leq n} |\lambda_k(\mathbf{q})|$ taken over the relevant range of \mathbf{q} . Depending on the region where the maximum is taken, there are two variations of the solver, the global and local Lax-Friedrichs solvers, both of which are used in the numerical section. Note that its local version is commonly referred to as the Rusanov flux. The HLL-type solvers are more complicated and the details are described in Appendix B. The HLL, HLLC and HLLD solvers are all experimented in this framework, and unsurprisingly the HLL and HLLC solvers are found to produce solutions better than the Lax-Friedrichs solver (the most dissipative one we test) and worse than the HLLD solver (the least dissipative one we test) for most benchmark problems. Therefore, to save the space, only the results of the Lax-Friedrichs and HLLD solvers are presented in the numerical section.

The remaining higher order terms in (12) are constructed using the physical flux \mathbf{f}_i at the grid points x_i . For instance, if some central differences are used, the approximations become

$$(15a) \quad \Delta x^2 \partial_x^2 \mathbf{f}|_{i+1/2} \approx \frac{1}{48} (-5\mathbf{f}_{i-2} + 39\mathbf{f}_{i-1} - 34\mathbf{f}_i - 34\mathbf{f}_{i+1} + 39\mathbf{f}_{i+2} - 5\mathbf{f}_{i+3}),$$

$$(15b) \quad \Delta x^4 \partial_x^4 \mathbf{f}|_{i+1/2} \approx \frac{1}{2} (\mathbf{f}_{i-2} - 3\mathbf{f}_{i-1} + 2\mathbf{f}_i + 2\mathbf{f}_{i+1} - 3\mathbf{f}_{i+2} + \mathbf{f}_{i+3}).$$

Both approximations in (15) give a truncation error of $\mathcal{O}(\Delta x^6)$, which guarantees a fifth order accuracy of the numerical flux (12). More discussions on those terms are given in Section 3.2.

The extension to multiple dimensions can be treated in a dimension-by-dimension fashion. For example, a system of hyperbolic conservation law in two dimensions takes the form

$$(16) \quad \partial_t \mathbf{q} + \partial_x \mathbf{f}(\mathbf{q}) + \partial_y \mathbf{g}(\mathbf{q}) = 0,$$

where \mathbf{q} is a vector function of t , x and y , and \mathbf{f} and \mathbf{g} are the fluxes in the x and y directions, respectively. On a uniform mesh with $x_i = i\Delta x$ and $y_j = j\Delta y$, the system (16) can be solved by using a semi-discrete scheme,

$$(17) \quad \partial_t \mathbf{q}_{\mathbf{i}} + \frac{1}{\Delta x} (\hat{\mathbf{f}}_{i+1/2,j} - \hat{\mathbf{f}}_{i-1/2,j}) + \frac{1}{\Delta y} (\hat{\mathbf{g}}_{i,j+1/2} - \hat{\mathbf{g}}_{i,j-1/2}) = 0,$$

where $\mathbf{i} = (i, j)$ is a multi-index, and $\hat{\mathbf{f}}$ and $\hat{\mathbf{g}}$ are numerical fluxes approximated similarly as in 1D case,

$$(18a) \quad \hat{\mathbf{f}}_{i+1/2,j} = \mathbf{F}(\mathbf{q}_{i+1/2,j}^-, \mathbf{q}_{i+1/2,j}^+) - \frac{1}{24} \Delta x^2 \partial_x^2 \mathbf{f}|_{i+1/2,j} + \frac{7}{5760} \Delta x^4 \partial_x^4 \mathbf{f}|_{i+1/2,j},$$

$$(18b) \quad \hat{\mathbf{g}}_{i+1/2} = \mathbf{G}(\mathbf{q}_{i,j+1/2}^-, \mathbf{q}_{i,j+1/2}^+) - \frac{1}{24} \Delta y^2 \partial_y^2 \mathbf{g}|_{i,j+1/2} + \frac{7}{5760} \Delta y^4 \partial_y^4 \mathbf{g}|_{i,j+1/2}.$$

Here $\mathbf{q}_{i+1/2,j}^\pm$ and $\mathbf{q}_{i,j+1/2}^\pm$ are obtained by one-dimensional WENO interpolations, and \mathbf{F} and \mathbf{G} are Riemann solvers corresponding to \mathbf{f} and \mathbf{g} .

3.2. Limiting the higher-order terms. In [41] the higher-order derivatives $\partial_x^2 \mathbf{f}|_{i+1/2}$ and $\partial_x^4 \mathbf{f}|_{i+1/2}$ are first expanded in terms of the derivatives of \mathbf{f} with respect to \mathbf{q} and spatial derivatives of \mathbf{q} , and central differences are then used for approximations. In [42] the central differences given in (15) are used to approximate the higher-order terms directly. In [41, 42], good performance of the resulting schemes is demonstrated through benchmark problems of the compressible Euler equations in hydrodynamics.

However, during the numerical experiment of the MHD equations, the linear approximations (15) are found to cause oscillations near a strong discontinuity, which could result into instabilities. Hence, an extra limiting procedure is needed to switch the high-order numerical flux (11) to a first-order flux for such a case, while the resulting scheme is required to retain high-order accuracy in smooth regions. In this work, the high order derivatives in (11) are multiplied by an additional limiter σ and the numerical flux (denoted by $\hat{\mathbf{f}}^\sigma$) becomes

$$(19) \quad \hat{\mathbf{f}}_{i+1/2}^\sigma = \mathbf{f}_{i+1/2} + \sigma_{i+1/2} \sum_{k=1}^{[(m-1)/2]} a_{2k} \Delta x^{2k} \partial_x^{2k} \mathbf{f}|_{i+1/2}.$$

Note that for the case of $m = 5$ used in the current work, σ needs to satisfy

$$(20) \quad \sigma_{i+1/2} = \begin{cases} 1 + \mathcal{O}(\Delta x^3), & \text{when } \mathbf{q} \text{ is smooth in the stencil } S_{i+1/2} = \{x_{i-2}, \dots, x_{i+3}\}, \\ \mathcal{O}(\Delta x^2), & \text{when } \mathbf{q} \text{ contains a strong discontinuity in } S_{i+1/2}. \end{cases}$$

To see the effect of such a limiter, we note that for smooth problems,

$$\hat{\mathbf{f}}_{i+1/2} - \hat{\mathbf{f}}_{i+1/2}^\sigma = (1 - \sigma_{i+1/2}) \sum_{k=1}^{[(m-1)/2]} a_{2k} \Delta x^{2k} \partial_x^{2k} \mathbf{f}|_{i+1/2} = C_{i+1/2} \Delta x^5.$$

Moreover, the high order derivatives $\partial_x^{2k} \mathbf{f}$ and the coefficient of the $\mathcal{O}(\Delta x^3)$ term in σ lead to a smooth coefficient of $C_{i+1/2}$, meaning $|C_{i+1/2} - C_{i-1/2}| = \mathcal{O}(\Delta x)$. Hence, a difference of (19) gives

$$\begin{aligned} \frac{\hat{\mathbf{f}}_{i+1/2}^\sigma - \hat{\mathbf{f}}_{i-1/2}^\sigma}{\Delta x} &= \frac{\hat{\mathbf{f}}_{i+1/2} - \hat{\mathbf{f}}_{i-1/2}}{\Delta x} - \frac{C_{i+1/2} \Delta x^5 - C_{i-1/2} \Delta x^5}{\Delta x} \\ &= \frac{\hat{\mathbf{f}}_{i+1/2} - \hat{\mathbf{f}}_{i-1/2}}{\Delta x} + \mathcal{O}(\Delta x^5), \end{aligned}$$

and it appears to be enough to maintain the fifth-order accuracy in (10). In the following, we use $\hat{\mathbf{f}}_{i+1/2}$ to represent $\hat{\mathbf{f}}_{i+1/2}^\sigma$ without special declaration.

Here we employ the parameter introduced in [13] to control the oscillations. The parameter, based on the idea of the WENO-Z scheme [11], is constructed from the smoothness indicators β_k in (38) from the WENO interpolation. In the process to obtain $\mathbf{q}_{i+1/2}^-$, we set

$$\sigma_{\max} = 1 + \frac{|\beta_0 - \beta_2|}{\epsilon + \min\{\beta_0, \beta_2\}}, \quad \sigma_{\min} = 1 + \frac{|\beta_0 - \beta_2|}{\epsilon + \max\{\beta_0, \beta_2\}},$$

where ϵ is a small positive number (taken to be 10^{-6} in all the numerical examples) to avoid division by zero. We can thus obtain a candidate for the coefficient σ by

$$\sigma^- = \frac{\sigma_{\min}}{\sigma_{\max}}.$$

A similar formula for $\mathbf{q}_{i+1/2}^+$ gives rise to another candidate σ^+ . We finally set

$$(21) \quad \sigma_{i+1/2} = \min\{\sigma^-, \sigma^+\}.$$

Using Taylor expansions, it is easy to verify the definition (21) satisfies the constraint (20). More details can be found in [11, 13].

3.3. Curvilinear coordinates. Here we provide a brief discussion of using curvilinear coordinates as the computational domain to solve a general hyperbolic system. Assume the coordinates $\mathbf{x} = (x, y)$ is related to the curvilinear coordinates $\mathbf{r} = (\xi, \eta)$ via a continuous coordinate transformation $\mathbf{x} = \mathbf{x}(\mathbf{r})$. As illustrated in Figure 1, a uniform mesh in the computational domain is typically used in our implementation.

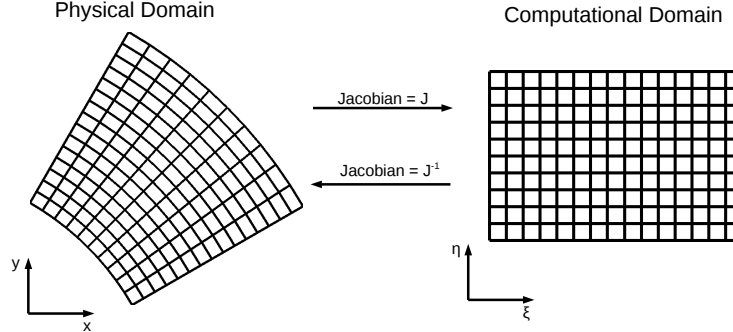


FIG. 1. A schematic diagram of the transformations between the physical and computational domain.

The two-dimensional system (16) in the curvilinear coordinates has a conservative form given by

$$(22) \quad \partial_t \tilde{\mathbf{q}} + \partial_\xi \tilde{\mathbf{f}} + \partial_\eta \tilde{\mathbf{g}} = 0,$$

where

$$(23) \quad \tilde{\mathbf{q}} = \frac{\mathbf{q}}{J}, \quad \tilde{\mathbf{f}} = \frac{1}{J}(\partial_x \xi \mathbf{f} + \partial_y \xi \mathbf{g}), \quad \tilde{\mathbf{g}} = \frac{1}{J}(\partial_x \eta \mathbf{f} + \partial_y \eta \mathbf{g}),$$

and J is the determinant of the Jacobian matrix defined by

$$J := \det \left[\frac{\partial \mathbf{r}}{\partial \mathbf{x}} \right],$$

which indicates $J^{-1} = \partial_\xi x \partial_\eta y - \partial_\eta x \partial_\xi y$. The standard metrics satisfy

$$\begin{aligned} \frac{\partial_x \xi}{J} &= \partial_\eta y, & \frac{\partial_y \xi}{J} &= -\partial_\eta x, \\ \frac{\partial_x \eta}{J} &= -\partial_\xi y, & \frac{\partial_y \eta}{J} &= \partial_\xi x. \end{aligned}$$

Note that the equation (22) in curvilinear coordinates is still hyperbolic. Therefore, the base scheme and other numerical treatments discussed previously can be applied straightforwardly on the uniform divided computational domain (ξ_i, η_j) after the numerical fluxes, \mathbf{f} and $\tilde{\mathbf{g}}$, are defined properly through (23). It has been suggested in [42] that to preserve the freestream condition, WENO interpolations should be applied to $\mathbf{q}(\mathbf{r})$ instead of $\tilde{\mathbf{q}}$. In the current work, we adopt this approach in the ideal MHD. In addition, the metrics $\partial_\xi x$, $\partial_\xi y$, $\partial_\eta x$ and $\partial_\eta y$ at half point are approximated by central differences given by

$$\begin{aligned} w|_{i+1/2,j} &= \frac{1}{256} (3w_{i-2,j} - 25w_{i-1,j} + 150w_{i,j} + 150w_{i+1,j} - 25w_{i+2,j} + 3w_{i+3,j}), \\ w|_{i,j+1/2} &= \frac{1}{256} (3w_{i,j-2} - 25w_{i,j-1} + 150w_{i,j} + 150w_{i,j+1} - 25w_{i,j+2} + 3w_{i,j+3}), \end{aligned}$$

with w stands the metrics, and have truncation errors $\mathcal{O}(\Delta\xi^6)$ and $\mathcal{O}(\Delta\eta^6)$, respectively. We note that the HLLD flux requires some non-trivial extensions on curvilinear meshes and the details are given in Appendix B.

4. Numerical approach in the ideal MHD.

4.1. Constrained transport. A constrained transport framework is used to control the divergence error of the magnetic field. In this framework, alongside evolving the conserved quantities of the ideal MHD equations, a magnetic vector potential \mathbf{A} , satisfying $\mathbf{B} = \nabla \times \mathbf{A}$, is evolved by

$$(24) \quad \partial_t \mathbf{A} + (\nabla \times \mathbf{A}) \times \mathbf{u} = 0.$$

This evolution equation is derived from the magnetic induction equation, see [50] for details. In the case of two dimensions considered in this work, the divergence-free condition (2) becomes

$$\nabla \cdot \mathbf{B} = \partial_x B_1 + \partial_y B_2 = 0.$$

It therefore suffices to only account for B_1 and B_2 in terms of controlling divergence errors in two dimensions. This leads to a nice property that only the third component of \mathbf{A} needs to be evolved. For ease of presentation, a scalar quantity, A , is used to denote the third component of \mathbf{A} . In 2D, the equation (24) leads to an evolution equation for A given by

$$(25) \quad \partial_t A + u \partial_x A + v \partial_y A = 0$$

and $\mathbf{B} = \nabla \times \mathbf{A}$ relates B_1 and B_2 with A by

$$B_1 = \partial_y A, \quad B_2 = -\partial_x A.$$

Many previous works show such a procedure can control the divergence error in \mathbf{B} and improve numerical stabilities of base schemes.

Same as our previous work [17], a WENO method designed for Hamilton-Jacobi equations [38] is modified to solve the potential equation (25). The approximation form is given by

$$(26) \quad \partial_t A_i = -u_i \left(\frac{\partial_x A_i^- + \partial_x A_i^+}{2} \right) - v_i \left(\frac{\partial_y A_i^- + \partial_y A_i^+}{2} \right) + \alpha_1 \left(\frac{\partial_x A_i^+ - \partial_x A_i^-}{2} \right) + \alpha_2 \left(\frac{\partial_y A_i^+ - \partial_y A_i^-}{2} \right),$$

where $\alpha_1 = \max_i |u_i|$ and $\alpha_2 = \max_i |v_i|$. Here $\partial_{x_m} A_i^\pm$ are defined by WENO reconstructions through

$$\begin{aligned} \partial_{x_m} A_i^- &:= \phi_{\text{WENO}}(D_{+x_m} A_{i-3,j}, D_{+x_m} A_{i-2,j}, D_{+x_m} A_{i-1,j}, D_{+x_m} A_{i,j}, D_{+x_m} A_{i+1,j}), \\ \partial_{x_m} A_i^+ &:= \phi_{\text{WENO}}(D_{+x_m} A_{i+2,j}, D_{+x_m} A_{i+1,j}, D_{+x_m} A_{i,j}, D_{+x_m} A_{i-1,j}, D_{+x_m} A_{i-2,j}), \end{aligned}$$

and D_{+x_m} is the standard forward difference defined by $D_{+x} A_i := (A_{i+1,j} - A_{i,j})/\Delta x$ and $D_{+y} A_i := (A_{i,j+1} - A_{i,j})/\Delta y$. The function ϕ_{WENO} is the classical fifth-order WENO reconstruction whose coefficients can be found in many previous works such as [17, 38, 39]. In the current multistage setting, the constrained transport is implemented through a predictor-corrector strategy, i.e., after the k -stage of the time integrator

at time t^{n+1} , the magnetic field is corrected by

$$B_{1,i}^{n+1,(k)} = \frac{A_{i,j-2}^{n+1,(k)} - 8A_{i,j-1}^{n+1,(k)} + 8A_{i,j+1}^{n+1,(k)} - A_{i,j+2}^{n+1,(k)}}{12\Delta y},$$

$$B_{2,i}^{n+1,(k)} = -\frac{A_{i-2,j}^{n+1,(k)} - 8A_{i-1,j}^{n+1,(k)} + 8A_{i+1,j}^{n+1,(k)} - A_{i+2,j}^{n+1,(k)}}{12\Delta x}.$$

Since the fourth-order central differences are used in the constrained transport step, the resulting scheme in this work is fourth-order. More details on the constrained transport using this approach can be found in the previous work [14, 17].

The potential A on curvilinear meshes are solved similarly. For instance, the evolution equation (25) in the curvilinear coordinates becomes

$$\partial_t A + (u \partial_x \xi + v \partial_y \xi) \partial_\xi A + (u \partial_x \eta + v \partial_y \eta) \partial_\eta A = 0,$$

which is solved by a discretization similar to (26) but approximated in the curvilinear coordinates. We note that while such discretization only guarantees the divergence-free condition of magnetic field to truncation errors on general curvilinear meshes, in practice we find this is sufficient to suppress the unphysical oscillations associated with the divergence error of \mathbf{B} .

4.2. A positivity-preserving limiter. During numerical experiments, we find that some HLL-type fluxes may cause the density or pressure becoming negative in some hard problems (such as the cloud-shock interaction in Section 5.5) even with the constrained transport step turned on. It appears to be related to the enhanced resolutions provided by the HLL-type solvers, since numerical solutions remain positive if the Lax-Friedrichs flux is used in the scheme. For such a case, a positivity-preserving limiter for ideal MHD equation in [16] is applied.

The limiter replaces the high-order flux $\hat{\mathbf{f}}_{i+\frac{1}{2}}$ constructed in (19) with a corrected flux $\hat{\mathbf{f}}_{i+\frac{1}{2}}^{\text{new}}$ given by

$$\hat{\mathbf{f}}_{i+\frac{1}{2}}^{\text{new}} = \theta_{i+\frac{1}{2}} \hat{\mathbf{f}}_{i+\frac{1}{2}} + (1 - \theta_{i+\frac{1}{2}}) \hat{\mathbf{f}}_{i+\frac{1}{2}}^{\text{low}},$$

where $\hat{\mathbf{f}}_{i+\frac{1}{2}}^{\text{low}}$ is a low-order flux which could preserve positive density and pressure, and the parameter $\theta_{i+\frac{1}{2}} \in [0, 1]$. The parameter $\theta_{i+\frac{1}{2}}$ is determined through solving a single optimization problem, which is derived from guaranteeing positivity of both density and pressure in the whole domain. It is very efficient to solve this optimization problem compared to the base scheme due to the construction of the parameter. The Lax-Friedrichs flux $\mathbf{f}_{i+\frac{1}{2}}$ given in (14) is typically used as the low-order flux $\hat{\mathbf{f}}_{i+\frac{1}{2}}^{\text{low}}$, with $\mathbf{q}^- = \mathbf{q}_i$ and $\mathbf{q}^+ = \mathbf{q}_{i+1}$. It has been proved that the limiter will guarantee positive numerical solutions if the low-order flux is positivity-preserving. For some simple problems such as scalar cases, it has been proved that a limiter using similar ideas achieves the designed accuracy of based schemes for smooth problems, see [15] for instance. For the ideal MHD equations, it has been numerically demonstrated in [14, 16] that the corrected flux maintains the designed order of accuracy of the high-order flux. For more details on the positivity-preserving limiter, see [14, 16, 51].

The implementation of the limiter on curvilinear meshes requires minor modifications. For instance, curvilinear meshes require solving the ideal MHD equation in the form of (22). Therefore, some steps of the limiter need to be modified accordingly. In the current multistage scheme, the limiter is applied at each stage. While in [16] it was sufficient to apply the limiter only at the final stage of each time step, we find it necessary to apply it at each stage in the current scheme. This, again, is possibly due to the enhanced resolution provided by the HLL-type fluxes.

4.3. Numerical boundary condition for PEC. In this section we derive a numerical boundary condition on a PEC boundary for the conserved quantities and the magnetic potential. A slip-wall numerical boundary condition for the Euler equations was given in [34] and a PEC numerical boundary condition for Maxwell's equations was given in [33]. Following the ideas in [33, 34], we derive a numerical PEC boundary condition for the ideal MHD equations. Note that the idea presented here is not limited to the PEC boundary condition for ideal MHD and it is extendible to some non-ideal MHD cases and other physical boundary conditions.

Without loss of generality, assume the PEC boundary is located at $\xi = \xi_0$. Its normal direction at the boundary is $\mathbf{n} = -\nabla_{\mathbf{x}}\xi/\|\nabla_{\mathbf{x}}\xi\|$. We further define the following quantities

$$\begin{aligned}\bar{u}_1 &:= \nabla_{\mathbf{x}}\xi \cdot (u, v)^T, & \bar{u}_2 &:= \nabla_{\mathbf{x}}\eta \cdot (u, v)^T, \\ \bar{B}_1 &:= \nabla_{\mathbf{x}}\xi \cdot (B_1, B_2)^T, & \bar{B}_2 &:= \nabla_{\mathbf{x}}\eta \cdot (B_1, B_2)^T,\end{aligned}$$

which are proportional to the components normal to curves ξ or η being constant, respectively. On a PEC boundary two normal components satisfy

$$(27) \quad \bar{u}_1(\xi_0, \eta, t) = 0,$$

$$(28) \quad \bar{B}_1(\xi_0, \eta, t) = 0.$$

Those are the only analytical boundary conditions needed on a PEC boundary. A local characteristic analysis reveals that there are one characteristic (forward fast magnetosonic waves) moving into the domain and one characteristic (backward fast magnetosonic waves) moving out, with the rest propagating along the boundary. Note that the magnetic boundary condition (28) is involved to guarantee four characteristics (Alfvén and slow magnetosonic waves) moving along the boundary. Therefore, these boundary conditions are still consistent with the local characteristic analysis, although there are two boundary conditions applied but only one characteristic moving in. Due to many characteristic moving parallel to the boundary, some careful treatments are needed to implement the conditions numerically.

Following the ideas in [34], we rely on the extrapolations and compatibility conditions to derive the numerical boundary condition with the help of ghost points. Based on the boundary condition (27) and (28) and the ideal MHD equations (1), a compatibility condition for the total pressure p_{tot} can be derived as

$$(29) \quad \partial_n p_{\text{tot}} = -\rho \bar{u}_2 \mathbf{n} \cdot \partial_\eta \mathbf{u} + \bar{B}_2 \mathbf{n} \cdot \partial_\eta \mathbf{B}.$$

It is a direct extension of the well-known compatibility condition for the Euler equations involving the normal derivative of the pressure along a curved slip wall. The details of the derivations are therefore omitted here.

Before discussing the numerical boundary conditions, we consider the analytical boundary condition for the magnetic potential A in the constrained transport framework. Along the boundary $\xi = \xi_0$, the magnetic boundary condition (28) gives

$$\bar{B}_1 = \partial_x \xi \partial_y A - \partial_y \xi \partial_x A = (\partial_x \xi \partial_y \eta - \partial_x \eta \partial_y \xi) \partial_\eta A = 0,$$

which further leads to

$$\partial_\eta A = 0.$$

Therefore, the potential at the boundary satisfies

$$\partial_t A + (u \partial_x \xi + v \partial_y \xi) \partial_\xi A = 0.$$

Due to $u \partial_x \xi + v \partial_y \xi = \nabla_{\mathbf{x}}\xi \cdot \mathbf{u}$ and the velocity boundary condition (27), the analytical boundary condition for the potential therefore is

$$(30) \quad A(\xi_0, \eta, t) = A^0,$$

with A^0 being some constant given in the initial condition.

Based on the above derivations for the PEC boundary, we propose a numerical compatibility boundary condition for the PEC boundary as follows. First, the velocities on the boundary are projected such that

$$\mathbf{n} \cdot \mathbf{u}_i = 0, \quad \mathbf{n} \cdot \mathbf{B}_i = 0, \quad \text{on } i = 0.$$

A Dirichlet boundary condition is applied to the magnetic potential

$$A_i = A^0, \quad \text{on } i = 0.$$

Note that the divergence in a general curvilinear coordinate can be written in a conservative form as

$$(31) \quad \nabla \cdot \mathbf{B} = J \sum_{m=1}^d \partial_{r_m} (\mathbf{a}_{r_m} \cdot \mathbf{B}), \quad \mathbf{a}_{r_m} = J^{-1} \nabla_{\mathbf{x}} r_m.$$

To implement the boundary condition numerically, 2nd-order discrete operators are defined as

$$D_{0\xi} q_i := \frac{q_{i+1,j} - q_{i-1,j}}{2\Delta\xi}, \quad D_{0\eta} q_i := \frac{q_{i,j+1} - q_{i,j-1}}{2\Delta\eta}.$$

Its normal derivative is defined as

$$D_{0n} q_i := \mathbf{n} \cdot (\partial_x \xi D_{0\xi} + \partial_x \eta D_{0\eta}, \partial_y \xi D_{0\xi} + \partial_y \eta D_{0\eta}) q_i.$$

The divergence-free condition can be used to determine the magnetic field in the normal direction as

$$(32) \quad D_{0\xi}(\mathbf{a}_\xi \cdot \mathbf{B}_i) = -D_{0\eta}(\mathbf{a}_\eta \cdot \mathbf{B}_i), \quad \text{on } i = 0.$$

The compatibility condition is used to determine the total pressure at the ghost points

$$(33) \quad D_{0n} p_{\text{tot},i} = -\rho_i \bar{u}_{2,i} \mathbf{n}_i \cdot D_{0\eta} \mathbf{u}_i + \bar{B}_{2,i} \mathbf{n}_i \cdot D_{0\eta} \mathbf{B}_i, \quad \text{on } i = 0.$$

Note that the conditions (32) and (33) are used to determine p_{tot} and the magnetic field $\mathbf{a}_\xi \cdot \mathbf{B}$ in the normal direction at $i = -1$. The same procedure can be used to determine those values at $i = -2$ and -3 if centered differences of wider stencils are used on the left-hand side of (32) and (33). In our implementation those approximations are all implemented in second-order for simplicity. The rest quantities $\{\rho, \mathbf{u}, B_t, B_3, A\}$ at the ghost points $i = -1, -2, -3$ are determined by extrapolations. Here B_t stands for the magnetic field in the transpose direction of the interface. The WENO extrapolation in [57] is used here as the limited extrapolation. For the quantity $q \in \{\rho, \mathbf{u}, B_t, B_3, A\}$, let

$$\begin{aligned} p_0(\xi) &= q_{0,j}, \\ p_1(\xi) &= \frac{q_{1,j} - q_{0,j}}{\Delta\xi} \xi + q_{0,j}, \\ p_2(\xi) &= \frac{q_{0,j} - 2q_{1,j} + q_{2,j}}{2\Delta\xi^2} \xi^2 + \frac{-3q_{0,j} + 4q_{1,j} - q_{2,j}}{2\Delta\xi} \xi + q_{0,j}, \end{aligned}$$

define the first, second and third-order extrapolations in the negative ξ direction, respectively. The limited extrapolation is defined by

$$\bar{p}(\xi) = \bar{\omega}_0 p_0(\xi) + \bar{\omega}_1 p_1(\xi) + \bar{\omega}_2 p_2(\xi),$$

where

$$\bar{\omega}_r = \frac{\bar{\alpha}_r}{\bar{\alpha}_0 + \bar{\alpha}_1 + \bar{\alpha}_2}, \quad \bar{\alpha}_r = \frac{\bar{d}_r}{(\bar{\beta}_r + \epsilon)^2}, \quad r = 0, 1, 2,$$

$\bar{d}_0 = \Delta\xi^2$, $\bar{d}_1 = \Delta\xi$ and $\bar{d}_2 = 1 - \Delta\xi - \Delta\xi^2$. The smoothness indicators here are given by

$$\bar{\beta}_0 = \Delta\xi^2, \quad \bar{\beta}_1 = (q_{1,j} - q_{0,j})^2, \quad \bar{\beta}_2 = \frac{13}{12}(q_{0,j} - 2q_{1,j} + q_{2,j})^2 + (2q_{0,j} - 3q_{1,j} + q_{2,j})^2.$$

More details can be found in [57] and note that β_2 therein contains a typo, which has been fixed here. We find this WENO extrapolation is slightly more robust than the limited extrapolation (a weighted average of first and third-order extrapolations) used in [34] for the current work.

Here the extrapolations are used to determine the transpose magnetic field B_t and B_3 . Note in [33] the boundary conditions for the electric fields are implemented differently by taking another time derivative of the evolution equations. However, for the MHD system we consider, it is easy to show that taking another

time derivative of the magnetic induction equation does not provide a useful constraint. The primary reason is that the electric field is fully determined by an ideal Ohm's law $\mathbf{E} = \mathbf{B} \times \mathbf{u}$ in the MHD system.

The idea of the compatibility boundary condition is similar to the idea of the so-called inverse Lax-Wendroff method [57]. Both methods convert the normal derivatives of certain variables to the tangential derivatives at the PEC or slip-wall boundary, see (32) and (33) for instance. To extend it to a boundary condition of higher order (higher than the second-order version presented here), the compatibility condition relies on high-order discrete operators of a wider stencil to approximate the conditions such as (32) and (33), which typically results into global coupling of all the ghost points, see [33] for instance. On the other hand, the inverse Lax-Wendroff approach relies on high-order time-derivatives to avoid global coupling, but for a PEC boundary condition considered here, such a procedure leads to very complicated algebraic relations. In practice, extrapolations are used to approximate those high-order time-derivatives, which may cause a new issue of numerical stabilities. Therefore, the extension to a higher-order boundary condition is challenging and remains an interesting line of future research.

In practice, a reflective boundary condition is typically used for the PEC boundary, see [20, 21] for instance. The boundary condition is simply implemented by copying the solution at the grid points (i, j) to the ghost points $(-i, j)$ and changing the sign of the velocity and magnetic field that are perpendicular to the interface. For the compressible Euler case, this boundary condition is only valid on straight walls and introduces a low-order error on curved walls, see [34] for instance. For the ideal MHD equations considered here, besides the same issue from hydrodynamics, another potential issue is that such a reflective magnetic field will also affect the divergence of the magnetic field and may lead to numerical instabilities for certain methods. In Section 5.8, we will use a bow shock benchmark to discuss those issues for high-order methods in further details.

5. Numerical results. In this section, numerical results are presented to demonstrate the accuracy and performance of the WENO scheme. For ease of reference, the WENO scheme based on the alternative flux formulation is simply referred to as the WENO scheme here. Since the schemes using different Riemann solvers produce similar solutions, we only present the numerical solutions using the Lax-Friedrichs and HLLD fluxes. Throughout the simulations, a third-order TVD-RK method is used as the time integrator. A CFL number of 0.5 is typically used, with the largest wave speed estimated in the curvilinear coordinates. Unless otherwise stated, the constrained transport and positivity-preserving limiter are turned on in numerical simulations, although those steps are not required for some easy problems.

5.1. 2D smooth Alfvén wave problem. We first consider the smooth Alfvén wave problem on a curvilinear mesh. This problem is used to verify the accuracy of the numerical schemes on general curvilinear meshes. The initial conditions is

$$(\rho, u, v, w, p, B_1, B_2, B_3)(0, x, y) = (1, 0, 0.1 \sin(2\pi x), 0.1 \cos(2\pi x), 0.1, 1, 0.1 \sin(2\pi x), 0.1 \cos(2\pi x)),$$

and its initial magnetic potential is

$$A(0, x, y) = y + 0.1 \frac{\cos(2\pi x)}{2\pi}.$$

The exact solution is an Alfvén wave propagating along x -direction with a wave speed of one.

In previous work such as [14, 17] the direction of the Alfvén wave was rotated so that it is not parallel to any grid lines in a Cartesian grid. In the current test, the same goal is achieved by keeping the direction of the wave parallel to x -direction but perturbing the Cartesian grid. The computational domain is set to be $(\xi, \eta) \in [0, 1]^2$, with the grid lines perturbed according to the mapping

$$\begin{aligned} x &= \xi + \epsilon_x \sin(2\pi \eta a_x), \\ y &= \eta + \epsilon_y \sin(2\pi \xi a_y), \end{aligned}$$

where ϵ_x and ϵ_y are the magnitude of perturbation and a_x and a_y are the wave numbers of the perturbation. In the results presented below, the parameters are taking by $\epsilon_x = 0.01$, $\epsilon_y = 0.02$, $a_x = 2$, and $a_y = 4$. As an illustration, a coarse grid of size 32×32 is presented in Figure 2. The boundary condition are all periodic for this smooth test.

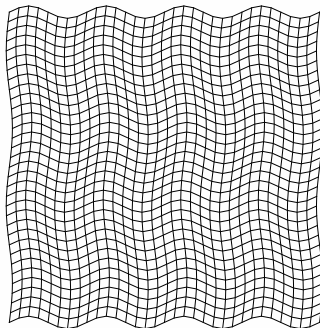


FIG. 2. Computational grid for the 2D Alfvén wave problem. The (coarse) grid is of size 32×32 in the computational domain of $(\xi, \eta) \in [0, 1]^2$ with $x = \xi + \epsilon_x \sin(2\pi \eta a_x)$ and $y = \eta + \epsilon_y \sin(2\pi \xi a_y)$.

TABLE 1
 L^∞ -errors of the 2D smooth Alfvén wave problem.

WENO with Lax-Friedrichs flux						
Mesh	Error in \mathbf{u}	Order	Error in \mathbf{B}	Order	Error in A	Order
32×32	3.324e-3	—	5.131e-3	—	1.560e-4	—
64×64	8.234e-5	5.34	4.090e-4	3.65	8.394e-6	4.22
128×128	6.713e-6	3.62	2.658e-5	3.94	5.266e-7	3.99
256×256	4.544e-7	3.88	1.677e-6	3.99	3.322e-8	3.99

WENO with HLLD flux						
Mesh	Error in \mathbf{u}	Order	Error in \mathbf{B}	Order	Error in A	Order
32×32	3.415e-3	—	5.257e-3	—	1.604e-4	—
64×64	8.260e-5	5.37	4.090e-4	3.68	8.388e-6	4.26
128×128	6.716e-6	3.62	2.658e-5	3.94	5.264e-7	3.99
256×256	4.542e-7	3.89	1.677e-6	3.99	3.322e-8	3.99

A refinement study is conducted on a sequence of grids of increasing resolution to verify the accuracy of the WENO methods with two Riemann solvers. The numerical solutions are compared to the exact solutions at $t = 1$. Throughout the refinement study, a fixed CFL number of 0.6 is used to determine the time step. Table 1 presents the L^∞ -errors of \mathbf{u} , \mathbf{B} and A and the estimated convergence rates. The error of the vector is the maximum taken over the Euclidean norm of the vector. The results are obtained using the WENO methods with the Lax-Friedrichs flux and the HLLD flux. The results confirm that the numerical schemes are both fourth-order accurate. Recall that a fourth-order constrained transport method is used and the resulting scheme in this work is fourth-order (in space). Note that the difference between the results of two fluxes is very small for this smooth problem. In the simulations, the constrained transport and positivity-preserving limiter are both turned on.

5.2. Brio-Wu shock tube. The second problem we consider is a commonly tested Riemann problem of the Brio-Wu shock tube test. The initial conditions in 1D are

$$(\rho, u, v, w, p, B_1, B_2, B_3) = \begin{cases} (1, 0, 0, 0, 1, 0.75, 1, 0) & \text{if } x < 0, \\ (0.125, 0, 0, 0, 0.1, 0.75, -1, 0) & \text{if } x \geq 0. \end{cases}$$

The schemes are first tested in 1D on both uniform and non-uniform meshes, and then they are tested on a 2D uniform mesh with the initial conditions rotated.

5.2.1. 1D shock tube. Figure 3 present the density on a uniform mesh of 200 grid points. The solutions of the WENO schemes with the Lax-Friedrichs (WENO-LF) and HLLD (WENO-HLLD) fluxes are presented. The results are compared to a reference solution on a very fine mesh solved using the scheme in [17]. The numerical results of two fluxes match well with the reference solution as well as other numerical results in the literature. As shown from the zoomed views in Figure 3, the numerical solutions of the HLLD flux show less smeared structures around the contact discontinuity, shock and compound waves. The solutions of the HLLD flux around rarefaction (not presented in the zoomed views) also show some improvements over

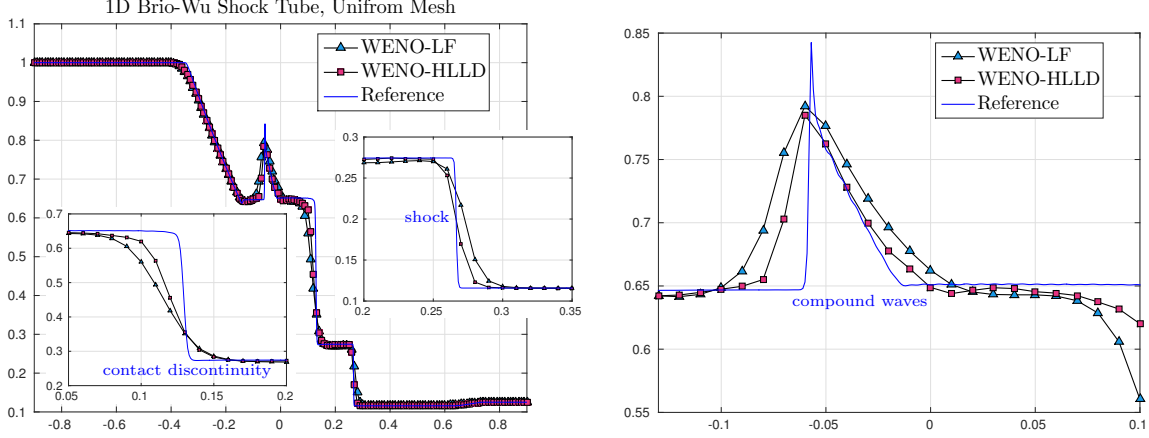


FIG. 3. 1D Brio-Wu shock tube. Density solved using the WENO schemes with two fluxes at $t = 0.2$ and its three zoomed views around the contact discontinuity, shock and compound waves. The solutions are computed on a uniform mesh of 200 points. The reference solution is a numerical solution on a fine mesh of 2000 points.

the solutions of the Lax-Friedrichs flux. This 1D results show the low-dissipative solver performs better in problems involving shocks or contact discontinuities.

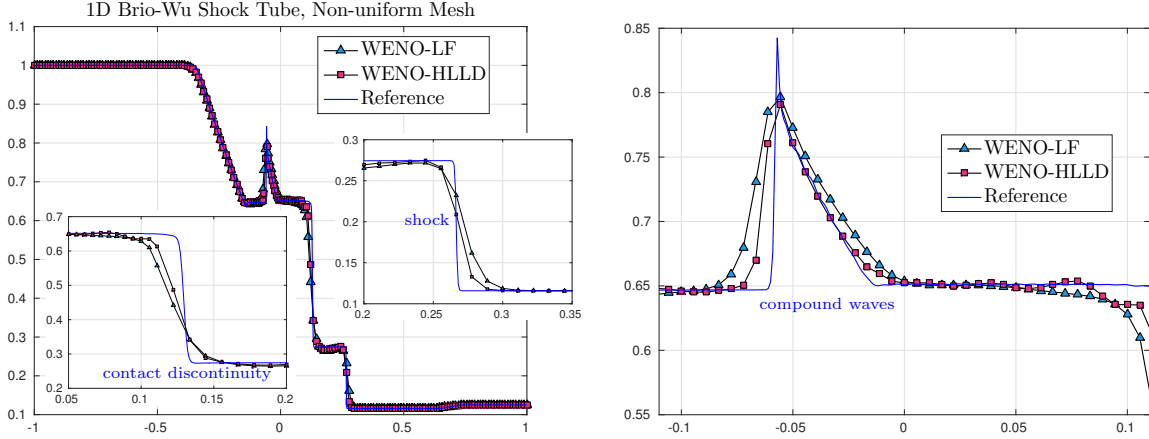


FIG. 4. 1D Brio-Wu shock tube. Density solved using the WENO schemes with two fluxes at $t = 0.2$ and its three zoomed views around the contact discontinuity, shock and compound waves. The solutions are computed on a non-uniform mesh of 200 points. The reference solution is a numerical solution on a fine mesh of 2000 points.

Next we examine the scheme on a non-uniform mesh given by the mapping

$$x = \begin{cases} \frac{5}{9}\xi & \text{if } |\xi| \leq 0.2, \\ \text{sign}(\xi) \left(\frac{1}{9} + \frac{10}{9} (|\xi| - 0.2) \right) & \text{otherwise,} \end{cases}$$

with $-1 \leq \xi \leq 1$. Note that the mesh is clustered around the region $[-0.11, 0.11]$ by a factor of $9/5$ and coarsened by a factor of 0.9 at the remaining region. Figure 4 presents the density on a non-uniform mesh of 200 grid points that are solved using the WENO schemes with two fluxes. The results are similar to the results on uniform meshes. The solutions also resolve the contact discontinuity and compound waves better due to the clustered grids points around those regions. We also note that both the WENO schemes can handle the abrupt change in the grid spacing of the non-uniform meshes.

5.2.2. 2D rotated shock tube. The Brio-Wu shock tube is then solved in 2D. As illustrated in Figure 5, the Riemann problem is rotated by an angle of $\tan^{-1}(0.5)$ with respect to x -direction. The computational domain is $[-1, 1] \times [-0.5, 0.5]$, an inflow boundary condition is used on the left and an outflow boundary condition is used on the right. The top and bottom boundary conditions are zero-order extrapolations along the tangential direction of the wave propagation for the conserved quantities and a

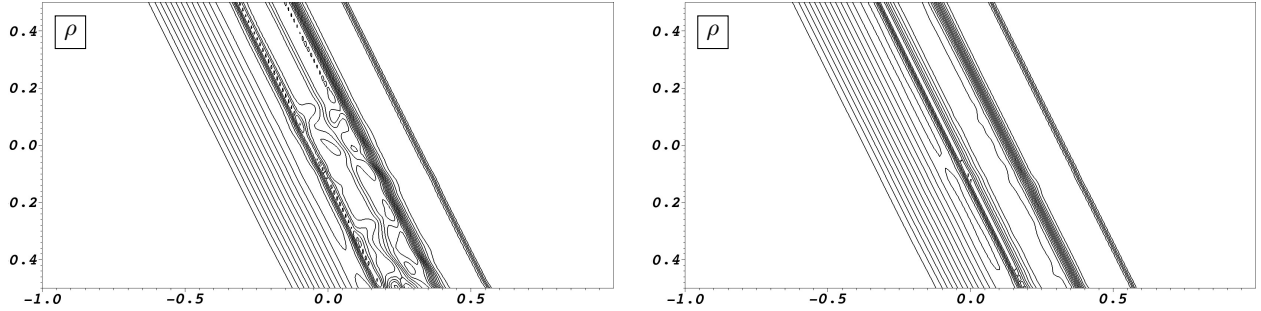


FIG. 5. 2D rotated Brio-Wu shock tube. Density at $t = 0.2$. Left: constrained transport and positivity-preserving limiter turned off. Right: constrained transport and positivity-preserving limiter turned on. The WENO scheme with the Lax-Friedrichs flux is used on a uniform grid of size 200×100 .

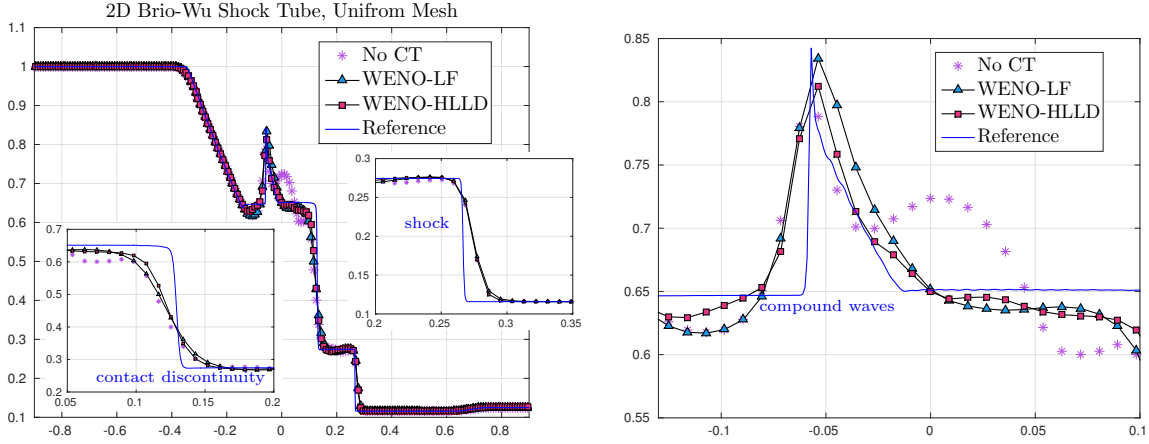


FIG. 6. 2D rotated Brio-Wu shock tube. Density solved using the WENO schemes at $t = 0.2$ and its three zoomed views around the contact discontinuity, shock and compound waves. The solutions are computed on a uniform mesh of size 200×100 . The reference solution is a numerical solution on a fine mesh of 2000 points.

linear extrapolation along the same direction is used for the potential. The results presented in this section use a uniform mesh of size 200×100 . Since the direction of the wave propagation is not parallel to the coordinate axes any more, this 2D Riemann problem requires the divergence-free condition to be handled properly. Figure 5 presents the contour plot of density solved using the WENO schemes with the Lax-Friedrichs flux. Note that there are spurious oscillations around the region of compound waves and contact discontinuity in the solutions using the scheme with the constrained transport step turned off. For a low-dissipative scheme, it is found that controlling the divergence error is even more important, since the scheme with the HLLD flux becomes unstable before t reaches the final time when the constrained transport step is turned off. Figure 6 shows the computed solutions along $y = 0$ that are projected to the direction of the wave propagation. The solution without the constrained transport step has some oscillations which are not observed in the solutions with the constrained transport step. The solutions of two schemes with the constrained transport step show a good agreement with the reference solution. It is observed that the solution of the HLLD flux is still better than the solution of the Lax-Friedrichs flux around the component waves and contact discontinuity, while the improvement are not so obvious around the shock region. The plausible reason is that the constrained transport step introduces extra dissipations around the shock. To reduce the dissipations from the constrained transport step in those shock regions can be a challenging task, since the dissipations may be important to maintain the stability of the schemes.

5.3. 2D field loop. In this section we consider a 2D advection of a weakly magnetized field loop from [26]. The initial conditions are

$$(\rho, u, v, w, p)(0, x, y) = \left(1, \sqrt{5} \cos(\theta), \sqrt{5} \sin(\theta), 0, 1\right)$$

with the advection angle of $\theta = \tan^{-1}(0.5)$. Magnetic field components are initialized by taking the curl of the magnetic potential A

$$A(0, x, y) = \begin{cases} 0.001(R - r), & \text{if } r \leq R, \\ 0, & \text{otherwise.} \end{cases}$$

with $r = \sqrt{x^2 + y^2}$ and $R = 0.3$. The example is solved on a stationary curve grid and a randomized grid. The curve grid is mapped from the computational domain $(\xi, \eta) \in [-1, 1] \times [-0.5, 0.5]$:

$$\begin{aligned} x &= \xi + \epsilon_x \sin(2\pi\eta), \\ y &= \eta + \epsilon_y \sin(2\pi\xi). \end{aligned}$$

where $\epsilon_x = -0.03$ and $\epsilon_y = -0.05$. The randomized grid is formed by randomizing the uniform computation domain (ξ, η) with 10% magnitude grid spacing $\Delta\xi$ or $\Delta\eta$ in a random direction. Periodic boundary conditions are used in both directions. In Figure 7, we present gray-scale images of $B_1^2 + B_2^2$ and contour plots of the potential A at $t = 2$, with 200×100 grid points. Note that the magnetic field maintains the circular symmetry of the loop as expected. The numerical dissipations are observed around the center and edge of the loop, which is similar to the results in [26]. Note that for this problem the schemes of different numerical fluxes produce almost identical results, since the solutions are essentially determined by the constrained transport step. Therefore, the results of the Lax-Friedrichs flux are not presented in Figure 7.

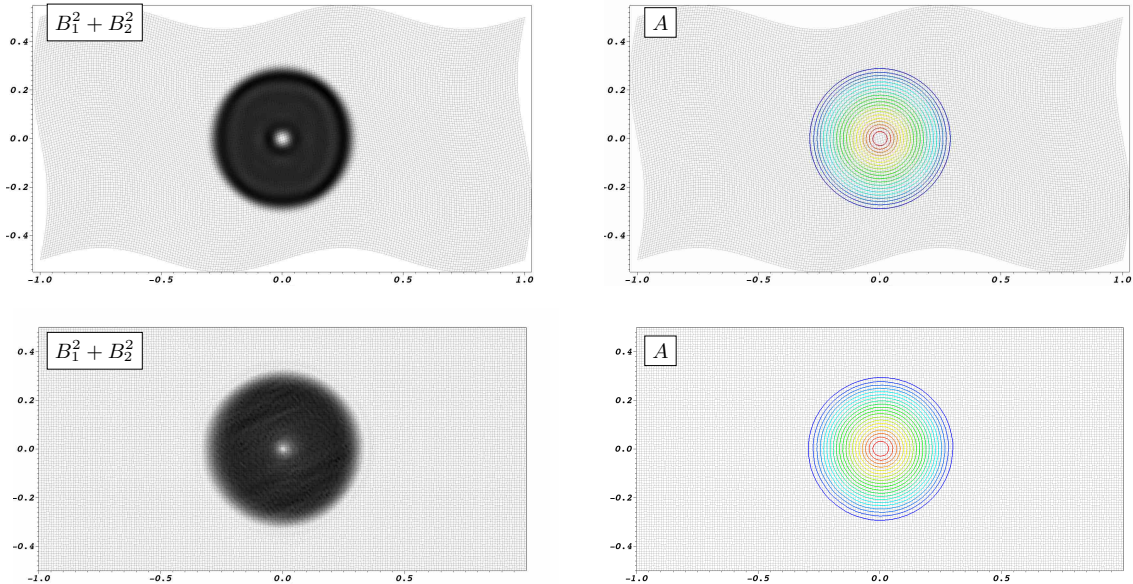


FIG. 7. 2D field loop. Top row: the solutions on the curve grid at $t = 2$. Bottom row: the solutions on the randomized grid at $t = 2$. The computational grids of size 200×100 are plotted (the light solid lines).

5.4. 2D Orszag-Tang vortex. We next consider a common benchmark problem of the 2D Orszag-Tang vortex problem. The initial conditions are

$$(\rho, u, v, w, p, B_1, B_2, B_3)(0, x, y) = (\gamma^2, -\sin(y), \sin(x), 0, \gamma, -\sin(y), \sin(2x), 0),$$

and its initial magnetic potential is

$$A(0, x, y) = 0.5 \cos(2x) + \cos(y).$$

To examine the performance of the schemes on general curvilinear meshes, a mesh similar to the one in Section 5.1 is used. In particular, the computational domain is $(\xi, \eta) \in [0, 2\pi] \times [0, 2\pi]$ and the curvilinear grid is given by the mapping

$$\begin{aligned} x &= \xi + \epsilon_x \sin(\eta a_x), \\ y &= \eta + \epsilon_y \sin(\xi a_y), \end{aligned}$$

where $\epsilon_x = 0.03$, $\epsilon_y = 0.05$, $a_x = 2$ and $a_y = 4$. The boundary conditions are all periodic.

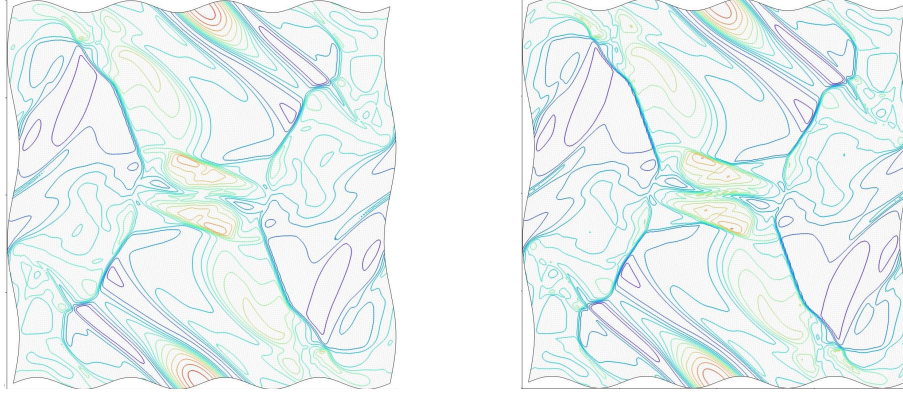


FIG. 8. Orszag-Tang vortex problem. Contour plots of density at $t = 3$ are presented with 15 equally spaced contour lines. A perturbed mesh of size 192×192 is used. Left: WENO with Lax-Friedrichs flux. Right: WENO with HLLD flux. The constrained transport step and positivity-preserving limiter are turned on.

Figure 8 presents the contour plots of the density at time $t = 3$. The solutions of two schemes are presented with 15 equally spaced contour lines. The problem starts from an smooth initial condition and develops an vortex and several MHD shock waves. Those waves interacts with each other (see Figure 8) and eventually result in turbulence. For such a problem, a low-dissipative scheme is preferred to capture small structures. It is observed from Figure 8 that the HLLD flux produces the less dissipative solutions, for instance, around the shock region. Although the previous Riemann problem test in Section 5.2 shows the dissipation from the constrained transport problem may smear those shocks, the current results show that the improvement of a low-dissipative scheme is still significant for practical problems, such as MHD turbulence simulations. The computed solutions match well with those found in the literature [17, 19, 50, 59, 61]. We note that the simulations run successfully to a much later time of $t = 10$, which indicates that the divergence-free condition is handled properly on a curvilinear mesh by the constrained transport approach. Without the constrained transport step, the simulations becomes unstable as soon as discontinuities develop in the solutions.

5.5. 2D cloud-shock interaction. In this section we consider the 2D cloud-shock interaction problem. The initial conditions are

$$\begin{aligned}
 & (\rho, u, v, w, p, B_1, B_2, B_3)(0, x, y) \\
 & = \begin{cases} (3.86859, 11.2536, 0, 0, 167.345, 0, 2.1826182, -2.1826182) & \text{if } x < 0.05, \\ (10, 0, 0, 0, 1, 0, 0.56418958, 0.56418958) & \text{if } x > 0.05, r < 0.15, \\ (1, 0, 0, 0, 1, 0, 0.56418958, 0.56418958) & \text{otherwise,} \end{cases}
 \end{aligned}$$

where $r = \sqrt{(x - 0.25)^2 + (y - 0.5)^2}$. The initial magnetic potential is,

$$A(0, x, y) = \begin{cases} -2.1826182 x + 0.080921431 & \text{if } x \leq 0.05, \\ -0.56418958 x & \text{if } x > 0.05. \end{cases}$$

The problem models an MHD shock propagating toward a dense bubble, resulting into very complex structures as the shock passes through the bubble. Those structures around the bubble are very sensitive to the numerical dissipations and low dissipative schemes are advantageous to obtain less smeared structures. Here we use this problem to study the effects of the Riemann solvers on both the Cartesian and curvilinear grids.

The problem is first solved on a square domain of $(x, y) \in [0, 1] \times [0, 1]$. A uniform Cartesian grid of size 256×256 is used with an inflow boundary condition applied at the left boundary and the outflow boundary condition applied at the other three boundaries. Figure 9 presents Schlieren plots of the logarithm of the density, norm of the magnetic field and pressure at $t = 0.06$. The solution matches well with the results in the literature, such as those in [14, 17, 19, 50]. It is observed that the HLLD flux resolves shocks and other

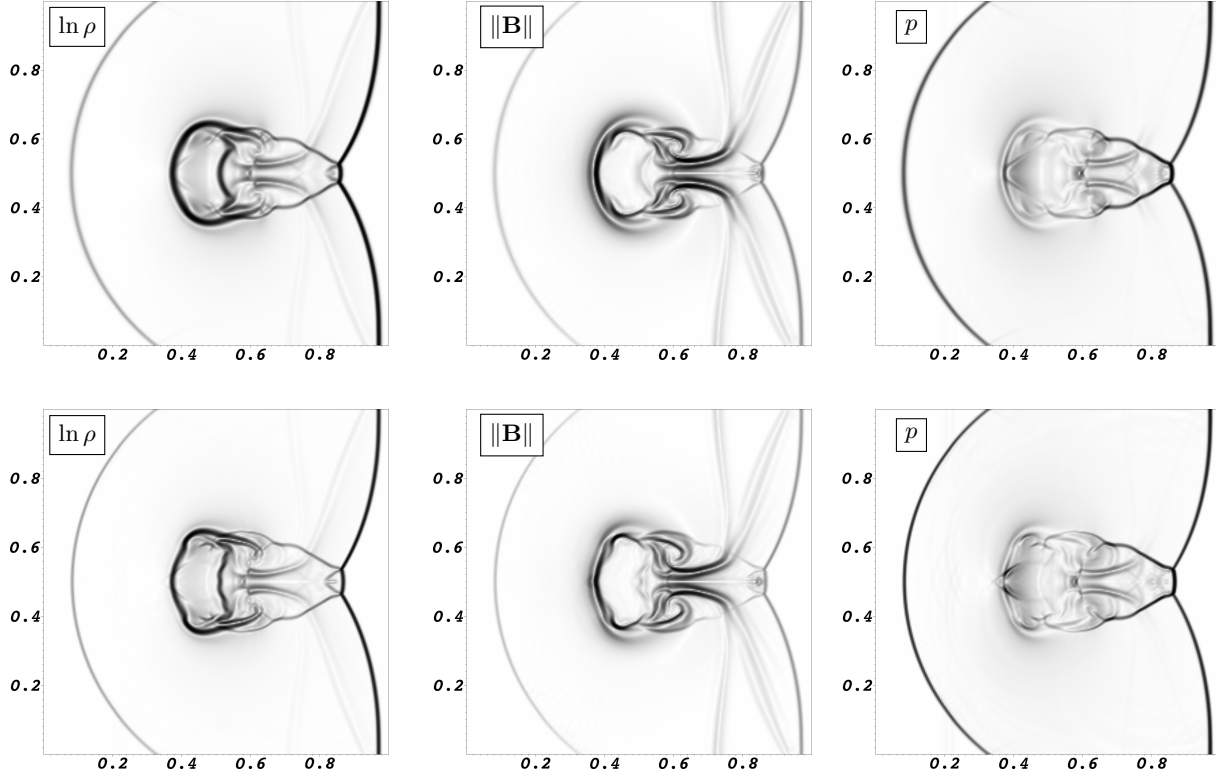


FIG. 9. 2D cloud-shock interaction. Schlieren plots of the logarithm of the density, norm of the magnetic field and pressure at $t = 0.06$. Top row: WENO with the Lax-Friedrichs flux. Bottom row: WENO with the HLLD flux. A uniform Cartesian grid of size 256×256 is used. The constrained transport step and positivity-preserving limiter are turned on.

complex features much better, although both schemes are fourth-order accurate and produce similar results in the smooth Alfvén wave test in Section 5.1. In particular, the complex structures around the initial bubble locations of the HLLD flux are less smeared than those in the Lax-Friedrichs flux.

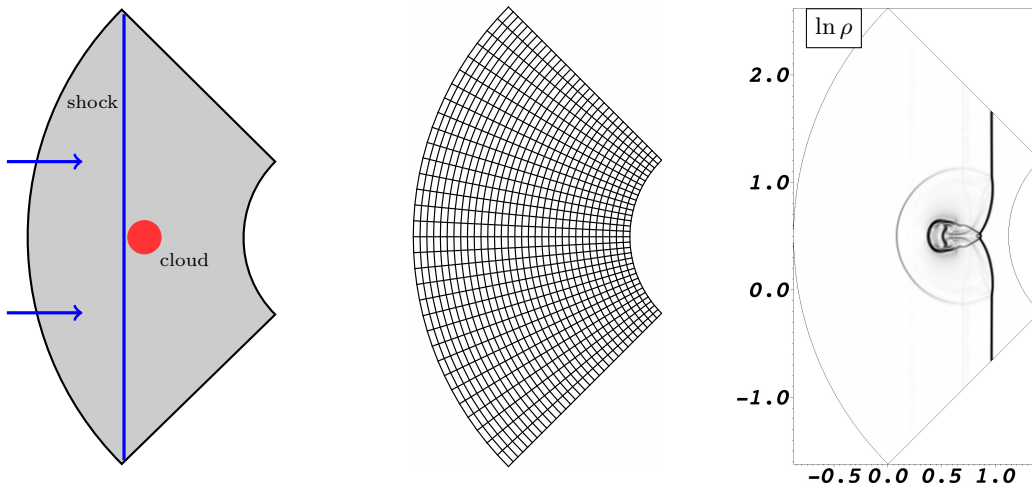


FIG. 10. Left: a diagram of the cloud-shock interaction in a sector domain. Middle: a coarse grid of size 32×32 . Right: the density at $t = 0.06$ on a fine grid of size 256×256 .

We next consider the same problem but change the physical domain to a sector region. As illustrated

in Figure 10, the domain is determined by the following mapping

$$\begin{aligned} x &= (3 - 2\xi) \cos(\pi + (1 - 2\eta)\pi/4) + 3 \cos(\pi/4), \\ y &= (3 - 2\xi) \sin(\pi + (1 - 2\eta)\pi/4) + 0.5, \end{aligned}$$

with $(\xi, \eta) \in [0, 1] \times [0, 1]$. A uniform grid in the computational domain (ξ, η) is used for simulations as illustrated in Figure 10. The same initial condition is used but the initial cloud becomes relatively smaller compared to the computational domain, which can be also seen in the plot of density in Figure 10. An inflow boundary condition applied at the left edge of the sector domain and the remaining boundary conditions are outflow.

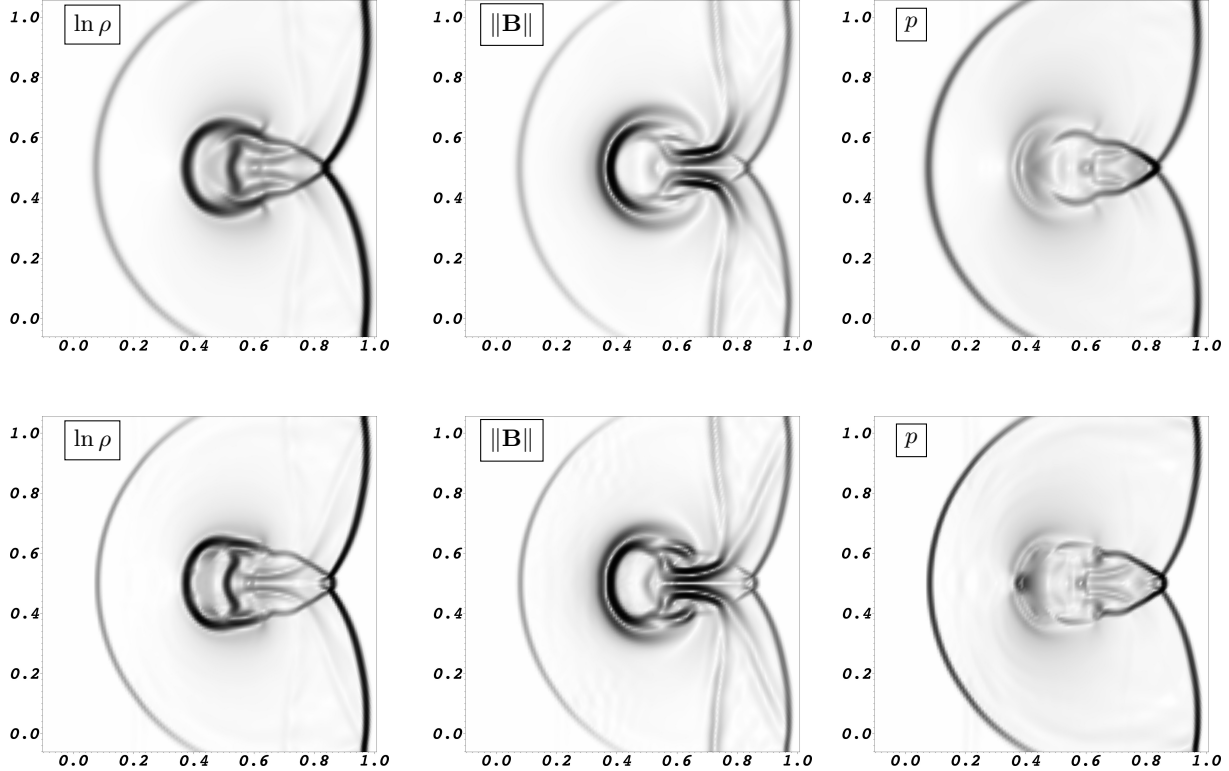


FIG. 11. 2D cloud-shock interaction. Schlieren plots of the logarithm of the density, norm of the magnetic field and pressure at $t = 0.06$. Top row: WENO with the Lax-Friedrichs flux. Bottom row: WENO with the HLLD flux. A curvilinear grid of size 256×256 is used. The constrained transport step and positivity-preserving limiter are turned on.

Figure 11 presents the results on the curvilinear grids. The presented results are Schlieren plots of the logarithm of the density, norm of the magnetic field and pressure. The presented results only focus on the region near the location of the initial cloud, which contains most interesting structures. The schemes with two numerical fluxes are used on a uniform grid of size 256×256 in the domain (ξ, η) . The results on the curvilinear grid are comparable to the results on the uniform grid, which verifies the solvers on general curvilinear grids. The HLLD flux also produces less smeared solutions. Note that the solutions on the curvilinear grid are more smeared because the effective grid spacing of the curvilinear grid is much larger than that of the Cartesian grid. Same as the Cartesian grid results, the HLLD flux also performs better than the Lax-Friedrichs flux in both the bubble region and shock region.

5.6. 2D rotor problem. The initial condition is given as

$$(\rho, u, v) = \begin{cases} (10, -(y - 0.5)/r_0, (x - 0.5)/r_0), & \text{if } r \leq r_0, \\ (1 + 9f(r), -f(r)(y - 0.5)/r, f(r)(x - 0.5)/r), & \text{if } r_0 < r \leq r_1, \\ (1, 0, 0), & \text{if } r > r_1, \end{cases}$$

and

$$w = 0, \quad B_1 = 2.5/\sqrt{4\pi}, \quad B_2 = 0, \quad B_3 = 0, \quad p = 0.5, \quad A = 2.5/\sqrt{4\pi y},$$

where $r = \sqrt{(x - 0.5)^2 + (y - 0.5)^2}$, $r_0 = 0.1$, $r_1 = 0.115$ and $f(r) = (r_1 - r)/(r_1 - r_0)$. Here we use the same initial condition of the second rotor problem test in [59]. The problem is solved on a stationary curve grid determined by the mapping

$$(34a) \quad x = \xi - 0.5 + \epsilon_x \cos(\pi(\eta - 0.5)) \sin(\pi(\xi - 0.5)),$$

$$(34b) \quad y = \eta - 0.5 + \epsilon_y \cos(\pi(\xi - 0.5)) \sin(\pi(\eta - 0.5)),$$

with $\epsilon_x = \epsilon_y = 0.1$ and $(\xi, \eta) \in [0, 1] \times [0, 1]$. The mach number at $t = 0.295$ on a grid of 256×256 are presented in Figure 12. From the zoomed view, we note that there is a significant improvement of the solutions computed by the HLLD flux.

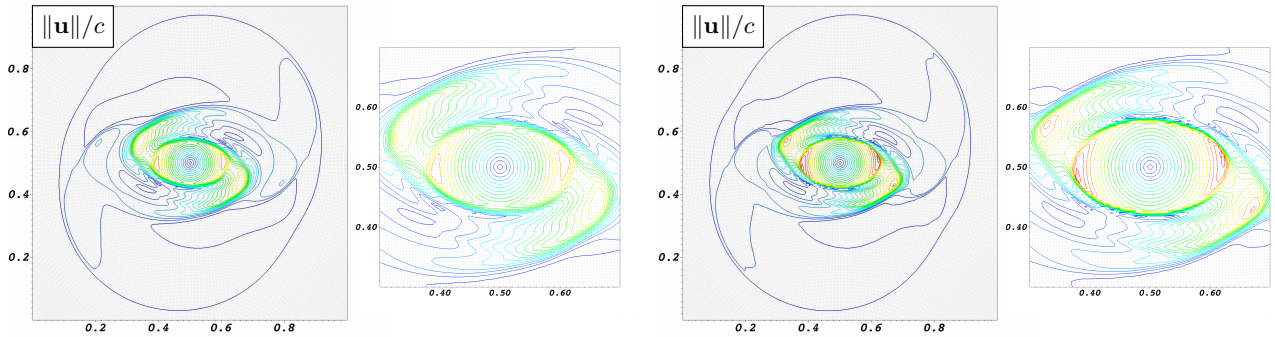


FIG. 12. 2D rotor problem. Contour plots of the mach number and their zoomed views are presented with 20 equally spaced contour lines in the range of $[0.12, 2.8]$. Left two: WENO with the Lax-Friedrichs flux. Right two: WENO with the HLLD flux. The computational grid of size 256×256 is plotted (the light solid lines).

5.7. 2D blast wave. Next we consider the blast wave problem in 2D. In this test strong shocks interact with a low- β background, which could potentially cause negative density or pressure in numerical simulations. The problem has been commonly used to test the positivity-preserving capabilities of numerical methods for MHD equation, see [7, 8, 16, 43] for instance. The initial conditions contain a constant density, velocity and magnetic field

$$(\rho, u, v, w, B_1, B_2, B_3)(0, x, y) = (1, 0, 0, 0, 50/\sqrt{2\pi}, 50/\sqrt{2\pi}, 0)$$

and a piecewise defined pressure

$$p(0, x, y) = \begin{cases} 1000, & \text{if } r \leq 0.1, \\ 0.1, & \text{otherwise,} \end{cases}$$

where r is the distance to the origin. The initial magnetic potential is

$$A(0, x, y) = 50/\sqrt{2\pi}(y - x).$$

Here we use the grid given in (34) and the boundary condition identical to the previous test in Section 5.6. Figure 13 shows the numerical solutions at $t = 0.01$ solved on a grid of 256×256 , which match well with the previous work. Note that the solutions of the HLLD flux are slightly less diffusive than the solutions of the Lax-Friedrichs flux.

5.8. Bow shock flow. We end our numerical investigation with a stationary bow shock flow. A bow shock flow benchmark has been previously considered in [20, 21, 47] but low-order finite volume methods were used therein. Here we use a similar problem to examine the performance of the WENO schemes when applied to problems involving curved physical boundaries. The compatibility boundary condition derived in Section 4.3 is also verified using this example.

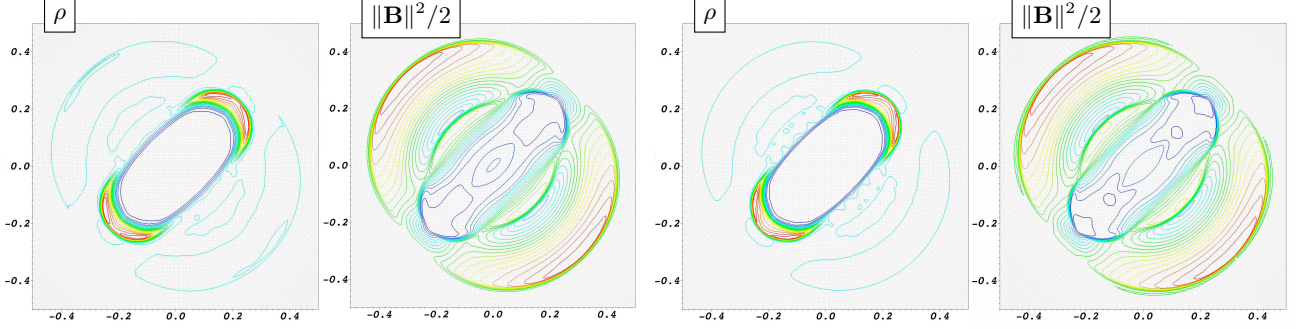


FIG. 13. 2D blast wave. Contour plots of the density and magnetic potential at $t = 0.01$ are presented with 20 equally spaced contour lines. Left two: WENO with the Lax-Friedrichs flux. Right two: WENO with the HLLD flux. The computational grid of size 256×256 is plotted (the light solid lines).

The computational domain is determined by the mapping

$$\begin{aligned} x &= (r_1 - (r_1 - r_0)\xi) \cos(\pi + (1 - 2\eta)\theta), \\ y &= (r_2 - (r_2 - r_0)\xi) \sin(\pi + (1 - 2\eta)\theta), \end{aligned}$$

with $r_1 = 0.3$, $r_2 = 0.65$, $r_0 = 0.125$, $\theta = 5\pi/12$ and $(\xi, \eta) \in [0, 1] \times [0, 1]$. A constant initial condition was used in [20, 21, 47] but it is not compatible with the PEC boundary initially. Typically, such a constant magnetic field will be first projected to satisfy the boundary condition in a solver but note that its projected field is not divergence-free. Although such a treatment is very common in the incompressible flow, it may cause some troubles for high-order methods in the MHD equations, since controlling divergence errors is more critical in the MHD equations. To avoid the potential issue, we modify the initial condition by ramping the constant magnetic field in a small annular region of distance $\delta r = 0.125$, so that both the PEC boundary and divergence-free condition are satisfied exactly in the initial condition. Assuming $r = \sqrt{x^2 + y^2}$, we impose an initial condition of $\rho = 1$, $p = 0.2$, $\mathbf{u} = (2, 0, 0)^T$ and the magnetic field

$$\mathbf{B} = \begin{cases} (B_1, B_2, 0)^T & \text{if } r \leq r_0 + \delta r, \\ (0.1, 0, 0)^T & \text{otherwise,} \end{cases}$$

with

$$\begin{aligned} B_1 &= 0.1 \frac{\pi y^2}{2 \delta r r} \cos\left(\frac{\pi(r - r_0)}{2 \delta r}\right) + 0.1 \sin\left(\frac{\pi(r - r_0)}{2 \delta r}\right), \\ B_2 &= -0.1 \frac{\pi x y}{2 \delta r r} \cos\left(\frac{\pi(r - r_0)}{2 \delta r}\right). \end{aligned}$$

The corresponding initial magnetic potential is

$$A = \begin{cases} 0.1 y \sin\left(\frac{\pi(r - r_0)}{2 \delta r}\right) & \text{if } r \leq r_0 + \delta r, \\ 0.1 y & \text{otherwise,} \end{cases}$$

The PEC boundary is applied at $\xi = 1$, i.e., $r = r_0$. An inflow boundary condition is applied at $\xi = 0$, and the outflow boundary condition is applied at the other two boundaries. A uniform grid of size 120×160 in the domain (ξ, η) is used for all the results presented in this section. Note that the results of this test are axisymmetric, and therefore we only present the results in the top half-plane.

It is found that if α in the Lax-Friedrichs flux (14) is estimated from the whole domain, the resultant value becomes too large for a reasonable CFL number in this case. This issue appears in the both WENO scheme and first-order scheme using the Lax-Friedrichs flux. Therefore, the local Lax-Friedrichs flux (the Rusanov flux) is used as one of two Riemann solvers tested for this problem. Note that the positivity-preserving limiter used in the previous examples relies on the fact that the low-order flux is positivity-preserving. But

for all the low-order fluxes (the local Lax-Friedrichs and HLL-type solvers) we test, a negative solution always appear for a CFL number larger than 0.2. Therefore, a slightly smaller CFL number of 0.2 is used in this case, which appears to be enough to eliminate numerical solutions becoming negative.

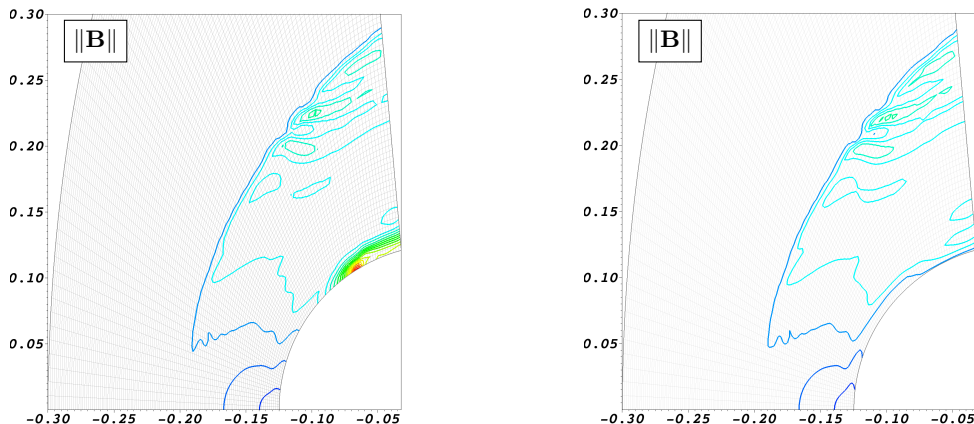


FIG. 14. *Bow shock flow. Contour plots of magnetic fields at $t = 0.28$ are presented with 20 equally spaced contour lines from $\|\mathbf{B}\| = 0$ to $\|\mathbf{B}\| = 0.7$. Left: the solution using the reflective boundary condition. Right: the solution using the compatibility boundary condition. The constrained transport step is not turned on.*

We first use this problem to study the numerical boundary condition for the PEC boundary. In previous work [20, 21], a reflective boundary condition was used and it produced a satisfactory results in those low-order finite volume methods. This fact has been confirmed in our own implementation, when the problem is simulated using the first-order numerical fluxes coupled with the forward Euler method. However, for the high-order methods derived in the current work, the reflective boundary condition generates a spurious magnetic field along the PEC surface. Figure 14 presents the magnetic fields at $t = 0.28$ generated by the reflective boundary condition and the compatibility boundary condition we derive in Section 4.3. Note that the magnetic field along the PEC surface is smooth for the solutions using the compatibility boundary condition while there is a large magnetic field generated along the surface in the results using the reflective boundary condition. This unphysical field becomes even larger as time evolves and eventually leads to a negative pressure, causing the failure of the solver around $t = 0.5$, while the solver using the compatibility boundary condition remains stable to produce a stationary bow shock profile, despite some oscillations due to divergence errors found near the shock front. Here the WENO scheme with a local Lax-Friedrichs flux is used with the constrained transport method turned off. The constrained transport method is not turned on for two reasons. First, the constrained transport method or other approaches to control the divergence errors, such as the non-conservative source terms used in the previous work [20, 21, 47], may diminish this issue to some extent, by introducing some dissipations to damp the divergence errors. In order to isolate different issues, those approaches are not used in the study of boundary conditions. Note that the base scheme using the compatibility condition is stable for the whole simulation, which clearly indicates the issue is not a direct consequence of the divergence error. Second, it is not clear how to implement a boundary condition for the potential which is consistent with the reflective boundary condition of the magnetic field.

The full benchmark problem is then simulated to obtain a stationary bow shock. As illustrate in Figure 14, the divergence errors can still lead to spurious oscillations around the bow shock front (see the contours around $y = 0.25$ for instance). For the results presented in Figure 15, the constrained transport step is turned on and the WENO schemes with the compatibility boundary condition are used to simulate the problem up to $t = 5$. The compatibility boundary condition for the potential described in Section 4.3 is also used for the PEC boundary. A steady bow shock profile are observed in the both density and magnetic field in Figure 15. The contour plots are complemented by the plots of several instantaneous streamlines (the dashed lines in the density plot), similarly to the previous work [20, 21, 47]. Our results match well with the results therein and the bow shock is much less smeared compared to their results. Note that the constrained transport method produces a much smoother profile of the magnetic field. During the simulations, it is found that the compatibility boundary condition may lead to a negative pressure at the ghost points, which does not require any extra care (note that the positivity-preserving limiter is not used in this case). The fundamental

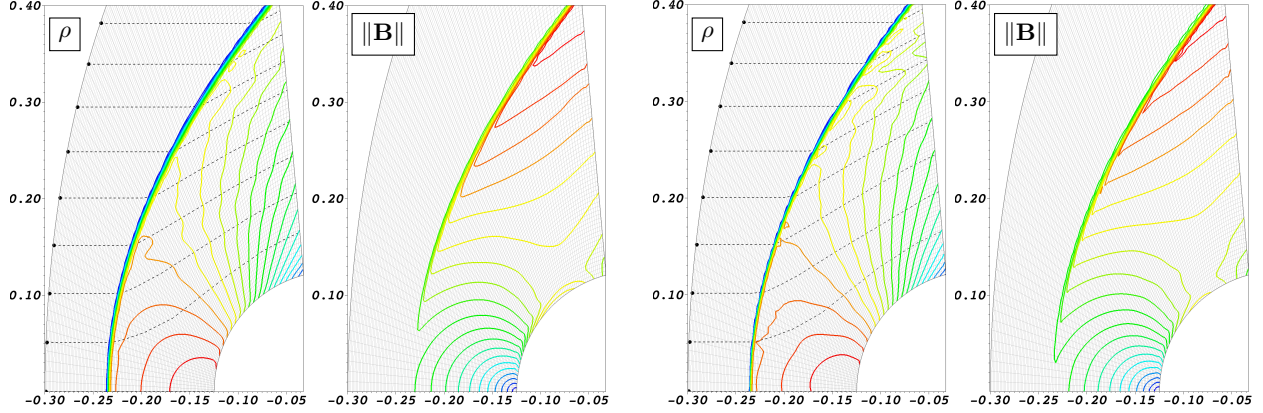


FIG. 15. *Bow shock flow. Contour plots of the density and magnetic field at $t = 5$ are presented with 20 equally spaced contour lines. The selected streamlines (the dashed lines) are added to the density plots. Left two: WENO with the Lax-Friedrichs flux. Right two: WENO with the HLLD flux. The computational grid of size 120×160 are also plotted (the light solid lines). The constrained transport step is turned on.*

reason is that the pressure computed from the step (33) is only used to convert the normal derivative of the pressure to the tangential derivatives along the surface. Since the pressure at ghost points are only used to construct the numerical fluxes, the negative pressure at those points will not cause the solutions at the computational domain become unphysical. Finally, the HLLD flux is also slightly advantageous over the local Lax-Friedrichs flux in terms of resolving the bow shock, but some oscillations are observed in its density plot, which is not surprising since the HLLD flux is much less dissipative.

6. Conclusions. In this work, we have extended an alternative flux formulation of the WENO scheme to the ideal MHD equations. Several Riemann solvers including a HLLD Riemann solver are used to approximate the leading (low-order) term in the numerical flux. The higher-order terms in the numerical flux are approximated by limited central differences of the physical flux and the limiter is based on the smoothness indicators in WENO interpolations. An unstaggered constrained transport method is used to control the divergence error of the magnetic field and a positivity-preserving limiter is implemented to increase the robustness of the scheme. The resulting scheme is applicable to general curvilinear meshes. To solve some benchmark problems involving a curved PEC boundary, we also derive a numerical compatibility boundary condition for both conserved quantities and magnetic potential.

Several numerical benchmark problems are used to validate the resultant scheme and to confirm the fourth-order accuracy of the scheme. The results show that when a low dissipative solver such as the HLLD solver is used in the base scheme, shocks and other complex features are much better captured than those in the solutions obtained using the base scheme with the Lax-Friedrichs solver. Through solving the benchmark problems on different meshes, we further demonstrate the robustness of the scheme on general curvilinear meshes. Using a bow shock flow benchmark, we confirm that the compatibility boundary condition produces a solution consistent with the solutions obtained by other low-order finite volume methods. It also demonstrates that a common implementation of the PEC boundary through a reflective boundary condition may cause failure of high-order methods.

There are several future directions for the current work. We are interested in extending the current scheme to three dimensions, which requires some work particularly in the constrained transport step. A compatibility boundary condition for a vector potential requires some careful derivations, in order to simulate a three-dimensional bow shock problem. In addition, a single-stage single-step scheme based on the alternative flux formulation of the WENO scheme can be further derived. Finally, the applications of the current scheme will be further explored in areas involving complex geometry.

Acknowledgements. We would like to thank Professor J.W. Banks for valuable discussions and comments.

Appendix A. WENO interpolation for a system.

For the sake of completeness, a WENO interpolation used in the current work is described for a hyperbolic system. Note that the WENO interpolation used here is performed on the local characteristic variables instead of on the components of \mathbf{q} . The resulting approximations to $\mathbf{q}_{i+1/2}^{\pm}$ are fifth-order accurate.

1. Compute an average state $\mathbf{q}_{i+1/2}$. In the current work, we use the arithmetic mean of primitive variables by setting $\psi_{i+1/2} = (\psi_i + \psi_{i+1})/2$ with ψ in the range of $\{\rho, \mathbf{u}, p, \mathbf{B}\}$, and the conserved variables $\mathbf{q} = \{\rho, \rho\mathbf{u}, \mathcal{E}, \mathbf{B}\}$ are then recovered from ψ .
2. Compute the right and left eigenvectors of the Jacobian $\partial\mathbf{f}/\partial\mathbf{q}$, and denote their matrices by

$$R_{i+1/2} = R(\mathbf{q}_{i+1/2}), \quad R_{i+1/2}^{-1} = R^{-1}(\mathbf{q}_{i+1/2}).$$

3. Project the conserved quantities \mathbf{q} , which is in the stencil of computing the numerical flux $\mathbf{f}_{i+1/2}$, to the local characteristic variables \mathbf{v} ,

$$(35) \quad \mathbf{v}_j = R_{i+1/2}^{-1} \mathbf{q}_j, \quad \text{for } j = i-2, \dots, i+3.$$

4. Perform a scalar WENO interpolation on each component of the characteristic variable \mathbf{v}_j to obtain the corresponding component of $\mathbf{v}_{i+1/2}^\pm$. Here, the procedure of a fifth-order WENO interpolation to obtain the k -th component $v_{k,i+1/2}^-$ is described:

- (a) Choose one big stencil as $S = \{x_{i-2}, \dots, x_{i+2}\}$, and three small stencils as $S^{(0)} = \{x_i, x_{i+1}, x_{i+2}\}$, $S^{(1)} = \{x_{i-1}, x_i, x_{i+1}\}$, and $S^{(2)} = \{x_{i-2}, x_{i-1}, x_i\}$. On those four stencils, the standard interpolation gives

$$(36a) \quad v_{k,i+1/2}^{(0)} = \frac{3}{8}v_{k,i} + \frac{3}{4}v_{k,i+1} - \frac{1}{8}v_{k,i+2},$$

$$(36b) \quad v_{k,i+1/2}^{(1)} = -\frac{1}{8}v_{k,i-1} + \frac{3}{4}v_{k,i} + \frac{3}{8}v_{k,i+1},$$

$$(36c) \quad v_{k,i+1/2}^{(2)} = \frac{3}{8}v_{k,i-2} - \frac{5}{4}v_{k,i-1} + \frac{15}{8}v_{k,i},$$

$$(36d) \quad v_{k,i+1/2}^{\text{big}} = d_0 v_{k,i+1/2}^{(0)} + d_1 v_{k,i+1/2}^{(1)} + d_2 v_{k,i+1/2}^{(2)},$$

with the linear weights being $d_0 = 5/16$, $d_1 = 5/8$ and $d_2 = 1/16$.

- (b) Compute nonlinear weights ω_r from the linear weights d_r ,

$$(37) \quad \omega_r = \frac{\alpha_r}{\alpha_0 + \alpha_1 + \alpha_2}, \quad \alpha_r = \frac{d_r}{(\beta_r + \epsilon)^2}, \quad r = 0, 1, 2,$$

where $\epsilon = 10^{-6}$ is used to avoid division by zero, and the *smoothness indicators* are given by

$$(38a) \quad \beta_0 = \frac{13}{12} (v_{k,i} - 2v_{k,i+1} + v_{k,i+2})^2 + \frac{1}{4} (3v_{k,i} - 4v_{k,i+1} + v_{k,i+2})^2,$$

$$(38b) \quad \beta_1 = \frac{13}{12} (v_{k,i-1} - 2v_{k,i} + v_{k,i+1})^2 + \frac{1}{4} (v_{k,i} - v_{k,i+1})^2,$$

$$(38c) \quad \beta_2 = \frac{13}{12} (v_{k,i-2} - 2v_{k,i-1} + v_{k,i})^2 + \frac{1}{4} (v_{k,i-2} - 4v_{k,i-1} + 3v_{k,i})^2.$$

- (c) The WENO interpolation is defined by

$$v_{k,i+1/2}^- = \sum_{r=0}^2 \omega_r v_{k,i+1/2}^{(r)}.$$

Note that the process to obtain $\mathbf{v}_{i+1/2}^+$ is mirror-symmetric to the procedure described above.

5. Finally, project $\mathbf{v}_{i+1/2}^\pm$ back to the conserved quantities,

$$(39) \quad \mathbf{q}_{i+1/2}^\pm = R_{i+1/2} \mathbf{v}_{i+1/2}^\pm.$$

Appendix B. HLL-type Riemann solvers for MHD equations.

Several HLL-type Riemann solvers for ideal MHD equations are described for the Riemann problem given by the initial conditions (4). Since the HLLD solver is an extension of the HLL and HLLC solvers, these two solvers are first reviewed in B.1 and B.2, and our version of the HLLD solver is then introduced in B.3. To save the space, the discussion here only focuses on the approximation solutions, and the corresponding numerical flux, which can be easily worked out, are therefore not described.

B.1. The HLL approximate Riemann solver. The approximate solution $\tilde{\mathbf{q}}$ in the HLL solver, consisting of three states, is given by

$$(40) \quad \tilde{\mathbf{q}}(t, \mathbf{x} \cdot \mathbf{n}) = \begin{cases} \mathbf{q}_L, & \text{if } (\mathbf{x} \cdot \mathbf{n})/t \leq S_L, \\ \mathbf{q}_{\text{HLL}}, & \text{if } S_L \leq (\mathbf{x} \cdot \mathbf{n})/t \leq S_R, \\ \mathbf{q}_R, & \text{if } S_R \leq (\mathbf{x} \cdot \mathbf{n})/t, \end{cases}$$

where S_L and S_R are the smallest and largest of all the signal speeds. The intermediate state satisfies

$$(41) \quad \mathbf{q}_{\text{HLL}} = \frac{S_R \mathbf{q}_R - S_L \mathbf{q}_L + \mathbf{F}_L - \mathbf{F}_R}{S_R - S_L},$$

which is given by the *consistency condition* of conservation laws

$$(42) \quad \int_{\xi_L}^{\xi_R} \tilde{\mathbf{q}}(t, \xi) d\xi = \xi_R \mathbf{q}_R - \xi_L \mathbf{q}_L + T(\mathbf{F}_L - \mathbf{F}_R),$$

with $\xi_L = TS_L$ and $\xi_R = TS_R$. \mathbf{q}_{HLL} is used in the numerical flux of the *subsonic* case where $S_L \leq 0 \leq S_R$.

B.2. The HLLC approximate Riemann solver. The approximate solution, consisting of two intermediate states connected by a contact discontinuity, is given by

$$(43) \quad \tilde{\mathbf{q}}(t, \mathbf{x} \cdot \mathbf{n}) = \begin{cases} \mathbf{q}_L, & \text{if } (\mathbf{x} \cdot \mathbf{n})/t \leq S_L, \\ \mathbf{q}_L^*, & \text{if } S_L \leq (\mathbf{x} \cdot \mathbf{n})/t \leq S_M, \\ \mathbf{q}_R^*, & \text{if } S_M \leq (\mathbf{x} \cdot \mathbf{n})/t \leq S_R, \\ \mathbf{q}_R, & \text{if } S_R \leq (\mathbf{x} \cdot \mathbf{n})/t, \end{cases}$$

where S_M is the estimated speed of an entropy wave, and \mathbf{q}_L^* and \mathbf{q}_R^* are the intermediate states. Consider the subsonic case where $S_L \leq 0 \leq S_R$. In [44] it was assumed

$$(44) \quad S_M = \mathbf{u}_L^* \cdot \mathbf{n} = \mathbf{u}_R^* \cdot \mathbf{n} = \mathbf{u}_{\text{HLL}} \cdot \mathbf{n},$$

$$(45) \quad p_{\text{totL}}^* = p_{\text{totR}}^*,$$

since the normal velocities and total pressures are same across a contact discontinuity. It was also assumed

$$(46) \quad \mathbf{B}_L^* \cdot \mathbf{n} = \mathbf{B}_R^* \cdot \mathbf{n} = \mathbf{B}_{\text{HLL}} \cdot \mathbf{n}.$$

Note that the RH condition (6) across S_α implies

$$(47) \quad S_\alpha \mathbf{q}_\alpha^* - \mathbf{F}_\alpha^* = S_\alpha \mathbf{q}_\alpha - \mathbf{F}_\alpha,$$

where $\alpha = L$ and R . Applying (47) to ρ gives $S_\alpha \rho_\alpha^* - \rho_\alpha^* \mathbf{u}_\alpha^* \cdot \mathbf{n} = S_\alpha \rho_\alpha - \rho_\alpha \mathbf{u}_\alpha \cdot \mathbf{n}$, which, with (44), implies

$$(48) \quad \rho_\alpha^* = \rho_\alpha \frac{S_\alpha - \mathbf{u}_\alpha \cdot \mathbf{n}}{S_\alpha - S_M}.$$

Applying (47) to $\rho \mathbf{u}$ gives

$$(49) \quad S_\alpha \rho_\alpha^* \mathbf{u}_\alpha^* - [\rho_\alpha^* (\mathbf{u}_\alpha^* \cdot \mathbf{n}) \mathbf{u}_\alpha^* + p_{\text{tot}\alpha}^* \mathbf{n} - (\mathbf{B}_\alpha^* \cdot \mathbf{n}) \mathbf{B}_\alpha^*] = S_\alpha \rho_\alpha \mathbf{u}_\alpha - [\rho_\alpha (\mathbf{u}_\alpha \cdot \mathbf{n}) \mathbf{u}_\alpha + p_{\text{tot}\alpha} \mathbf{n} - (\mathbf{B}_\alpha \cdot \mathbf{n}) \mathbf{B}_\alpha].$$

Taking the normal component of (49) and using (48) give

$$(50) \quad p_{\text{tot}\alpha}^* = p_{\text{tot}\alpha} + \rho_\alpha (S_\alpha - \mathbf{u}_\alpha \cdot \mathbf{n}) (S_M - \mathbf{u}_\alpha \cdot \mathbf{n}) + (\mathbf{B}_\alpha^* \cdot \mathbf{n})^2 - (\mathbf{B}_\alpha \cdot \mathbf{n})^2.$$

Using the assumption (44) to eliminate $\mathbf{u}_\alpha^* \cdot \mathbf{n}$ in (49) gives

$$(51) \quad \rho_\alpha^* \mathbf{u}_\alpha^* = \frac{\rho_\alpha \mathbf{u}_\alpha (S_\alpha - \mathbf{u}_\alpha \cdot \mathbf{n}) + (p_{\text{tot}\alpha}^* - p_{\text{tot}\alpha}) \mathbf{n} + (\mathbf{B}_\alpha \cdot \mathbf{n}) \mathbf{B}_\alpha - (\mathbf{B}_\alpha^* \cdot \mathbf{n}) \mathbf{B}_\alpha^*}{S_\alpha - S_M}$$

Similarly, applying (47) to \mathcal{E} and using the assumption (44) give

$$(52) \quad \mathcal{E}_\alpha^* = \frac{\mathcal{E}_\alpha(S_\alpha - \mathbf{u}_\alpha \cdot \mathbf{n}) + p_{\text{tot}\alpha}^* S_M - p_{\text{tot}\alpha}(\mathbf{u}_\alpha \cdot \mathbf{n}) + (\mathbf{B}_\alpha \cdot \mathbf{n})(\mathbf{B}_\alpha \cdot \mathbf{u}_\alpha) - (\mathbf{B}_\alpha^* \cdot \mathbf{n})(\mathbf{B}_\alpha^* \cdot \mathbf{u}_\alpha^*)}{S_\alpha - S_M}.$$

Here \mathbf{B}_α^* still needs to be determined. Note that the consistency condition in the HLLC solver gives

$$(53) \quad \frac{S_M - S_L}{S_R - S_L} \mathbf{q}_L^* + \frac{S_R - S_M}{S_R - S_L} \mathbf{q}_R^* = \mathbf{q}_{\text{HLL}}.$$

Applying it to $\rho \mathbf{u}$ and using (41) and (45) give $(\mathbf{B}_L^* \cdot \mathbf{n})\mathbf{B}_L^* = (\mathbf{B}_R^* \cdot \mathbf{n})\mathbf{B}_R^*$. Therefore, [44] suggested to set

$$(54) \quad \mathbf{B}_L^* = \mathbf{B}_R^* = \mathbf{B}_{\text{HLL}}.$$

Finally, the intermediate states are completely determined by (44), (48), (50), (51), (52) and (54).

B.3. The HLLD approximate Riemann solver. In the previous version of the HLLD Riemann solver [46], it was assumed that the normal vector to the discontinuity interface is parallel to one of the coordinate axes and the magnetic field components normal to the discontinuity interface are identical across the discontinuity. Neither of the assumptions holds on a curvilinear mesh. Therefore, we consider Riemann problems with the initial conditions (4) where the normal vector \mathbf{n} to the discontinuity interface may not be parallel to the coordinate axes and there are jumps in the normal magnetic field. Note that the divergence-free condition in multiple dimensions can be saved by the jumps in the tangential directions. We present our version of the HLLD solver that can handle these issues. The approximate solution, consisting of four intermediate states which are connected by two rotational discontinuities and one contact or tangential discontinuity, is given by

$$(55) \quad \tilde{\mathbf{q}}(t, \mathbf{x} \cdot \mathbf{n}) = \begin{cases} \mathbf{q}_L, & \text{if } (\mathbf{x} \cdot \mathbf{n})/t \leq S_L, \\ \mathbf{q}_L^*, & \text{if } S_L \leq (\mathbf{x} \cdot \mathbf{n})/t \leq S_L^*, \\ \mathbf{q}_L^{**}, & \text{if } S_L^* \leq (\mathbf{x} \cdot \mathbf{n})/t \leq S_M, \\ \mathbf{q}_R^{**}, & \text{if } S_M \leq (\mathbf{x} \cdot \mathbf{n})/t \leq S_R^*, \\ \mathbf{q}_R^*, & \text{if } S_R^* \leq (\mathbf{x} \cdot \mathbf{n})/t \leq S_R, \\ \mathbf{q}_R, & \text{if } S_R \leq (\mathbf{x} \cdot \mathbf{n})/t, \end{cases}$$

where S_L^* and S_R^* are the estimated speeds of rotational discontinuities, and S_M is the estimated speed of a contact or tangential discontinuity.

We first consider the subsonic case. Following the assumptions (44)–(46), we similarly assume

$$(56) \quad S_M = \mathbf{u}_L^* \cdot \mathbf{n} = \mathbf{u}_L^{**} \cdot \mathbf{n} = \mathbf{u}_R^{**} \cdot \mathbf{n} = \mathbf{u}_R^* \cdot \mathbf{n} = \mathbf{u}_{\text{HLL}} \cdot \mathbf{n},$$

$$(57) \quad p_{\text{tot}L}^* = p_{\text{tot}L}^{**} = p_{\text{tot}R}^{**} = p_{\text{tot}R}^*,$$

$$(58) \quad \mathbf{B}_L^* \cdot \mathbf{n} = \mathbf{B}_L^{**} \cdot \mathbf{n} = \mathbf{B}_R^{**} \cdot \mathbf{n} = \mathbf{B}_R^* \cdot \mathbf{n} = \mathbf{B}_{\text{HLL}} \cdot \mathbf{n}.$$

Recall that rotational discontinuities are linearly degenerate and correspond to the Alfvén waves of speed $\mathbf{u} \cdot \mathbf{n} \mp \sqrt{(\mathbf{B} \cdot \mathbf{n})^2 / \rho}$. Since densities are identical across rotational discontinuities, their speeds are

$$(59) \quad S_\alpha^* = S_M \mp \sqrt{(\mathbf{B}_{\text{HLL}} \cdot \mathbf{n})^2 / \rho_\alpha^*},$$

where $-$ and $+$ correspond to $\alpha = L$ and R respectively. Note that the four-intermediate-state solution (55) degenerates to a two-intermediate-state solution when either S_α^* is close to S_α for $\alpha = L$ and R , or S_L^* and S_R^* are both close to S_M , in which case the HLLD solver degenerates to the HLLC solver and no extra cares are needed. Note ρ_α^* can be determined similarly to (48) and remains the same as

$$(60) \quad \rho_\alpha^* = \rho_\alpha \frac{S_\alpha - \mathbf{u}_\alpha \cdot \mathbf{n}}{S_\alpha - S_M}.$$

Now consider the non-degenerate case when all the speeds are sufficiently spread apart. We first obtain \mathbf{q}_α^* from the RH condition across S_α . (50) and (51) also remain the same as

$$(61) \quad p_{\text{tot}\alpha}^* = p_{\text{tot}\alpha} + \rho_\alpha(S_\alpha - \mathbf{u}_\alpha \cdot \mathbf{n})(S_M - \mathbf{u}_\alpha \cdot \mathbf{n}) + (\mathbf{B}_\alpha^* \cdot \mathbf{n})^2 - (\mathbf{B}_\alpha \cdot \mathbf{n})^2,$$

$$(62) \quad \rho_\alpha^* \mathbf{u}_\alpha^* = \frac{\rho_\alpha(S_\alpha - \mathbf{u}_\alpha \cdot \mathbf{n}) + (p_{\text{tot}\alpha}^* - p_{\text{tot}\alpha})\mathbf{n} + (\mathbf{B}_\alpha \cdot \mathbf{n})\mathbf{B}_\alpha - (\mathbf{B}_\alpha^* \cdot \mathbf{n})\mathbf{B}_\alpha^*}{S_\alpha - S_M}.$$

Applying the RH condition across S_α to \mathbf{B} gives

$$(63) \quad S_\alpha \mathbf{B}_\alpha^* - [(\mathbf{u} \cdot \mathbf{n})\mathbf{B} - (\mathbf{B} \cdot \mathbf{n})\mathbf{u}]_\alpha^* = S_\alpha \mathbf{B}_\alpha - [(\mathbf{u} \cdot \mathbf{n})\mathbf{B} - (\mathbf{B} \cdot \mathbf{n})\mathbf{u}]_\alpha.$$

Here the notation $[\cdot]_\alpha^*$ stands for the flux of the corresponding solution state. The equations (62) and (63) form a linear system for \mathbf{u}_α^* and \mathbf{B}_α^* , and the solutions are

$$(64) \quad \mathbf{u}_\alpha^* = \left[\left((\mathbf{B}_\alpha \cdot \mathbf{n})(S_\alpha - S_M) - (\mathbf{B}_{\text{HLL}} \cdot \mathbf{n})(S_\alpha - \mathbf{u}_\alpha \cdot \mathbf{n}) \right) \mathbf{B}_\alpha \right. \\ \left. + \left(\rho_\alpha(S_\alpha - \mathbf{u}_\alpha \cdot \mathbf{n})(S_\alpha - S_M) - (\mathbf{B}_{\text{HLL}} \cdot \mathbf{n})(\mathbf{B}_\alpha \cdot \mathbf{n}) \right) \mathbf{u}_\alpha + (p_{\text{tot}\alpha}^* - p_{\text{tot}\alpha})(S_\alpha - S_M)\mathbf{n} \right] / D,$$

$$(65) \quad \mathbf{B}_\alpha^* = \left[\left(\rho_\alpha(S_\alpha - \mathbf{u}_\alpha \cdot \mathbf{n})^2 - (\mathbf{B}_{\text{HLL}} \cdot \mathbf{n})(\mathbf{B}_\alpha \cdot \mathbf{n}) \right) \mathbf{B}_\alpha \right. \\ \left. + \left(\rho_\alpha(S_\alpha - \mathbf{u}_\alpha \cdot \mathbf{n})(\mathbf{B}_\alpha \cdot \mathbf{n} - \mathbf{B}_{\text{HLL}} \cdot \mathbf{n}) \right) \mathbf{u}_\alpha - (p_{\text{tot}\alpha}^* - p_{\text{tot}\alpha})(\mathbf{B}_{\text{HLL}} \cdot \mathbf{n})\mathbf{n} \right] / D,$$

with $D = \rho_\alpha(S_\alpha - \mathbf{u}_\alpha \cdot \mathbf{n})(S_\alpha - S_M) - (\mathbf{B}_{\text{HLL}} \cdot \mathbf{n})^2$. Applying the RH condition across S_α to \mathcal{E} gives

$$(66) \quad \mathcal{E}_\alpha^* = \frac{\mathcal{E}_\alpha(S_\alpha - \mathbf{u}_\alpha \cdot \mathbf{n}) + p_{\text{tot}\alpha}^* S_M - p_{\text{tot}\alpha}(\mathbf{u}_\alpha \cdot \mathbf{n}) + (\mathbf{B}_\alpha \cdot \mathbf{n})(\mathbf{B}_\alpha \cdot \mathbf{u}_\alpha) - (\mathbf{B}_\alpha^* \cdot \mathbf{n})(\mathbf{B}_\alpha^* \cdot \mathbf{u}_\alpha^*)}{S_\alpha - S_M},$$

which has the same form as (52). Note that whereas the consistency condition (53) on $\rho\mathbf{u}$ is used to obtain \mathbf{B}_α^* in the HLLC solver, here the RH condition across S_α is applied to $\rho\mathbf{u}$ and \mathbf{B} for determining $\rho\mathbf{u}_\alpha^*$ and \mathbf{B}_α^* , and a consistency condition similar to (53) is saved for determining $(\rho\mathbf{u})_\alpha^{**}$ and \mathbf{B}_α^{**} later.

Next consider the inner intermediate states \mathbf{q}_α^{**} . Applying the RH condition across S_α^* to ρ gives $S_\alpha^* \rho_\alpha^{**} - (\rho\mathbf{u})_\alpha^{**} \cdot \mathbf{n} = S_\alpha^* \rho_\alpha^* - (\rho\mathbf{u})_\alpha^* \cdot \mathbf{n}$, which, with (56), gives

$$(67) \quad \rho_\alpha^{**} = \rho_\alpha^*.$$

Note that this is consistent with the fact that densities are identical across rotational discontinuities, which is assumed in deriving the estimates of S_L^* and S_R^* in (59). Since S_L^* and S_R^* are sufficiently spread apart, we assume $\mathbf{B}_{\text{HLL}} \cdot \mathbf{n} \neq 0$. Therefore, applying the RH condition across S_M to $\rho\mathbf{u}$ implies $\mathbf{B}_L^{**} = \mathbf{B}_R^{**}$ and applying it to \mathbf{B} implies $\mathbf{u}_L^{**} = \mathbf{u}_R^{**}$. Note that the consistency condition here becomes

$$(68) \quad (S_R - S_R^*)\mathbf{q}_R^* + (S_R^* - S_M)\mathbf{q}_R^{**} + (S_M - S_L^*)\mathbf{q}_L^{**} + (S_L^* - S_L)\mathbf{q}_L^* - S_R\mathbf{q}_R + S_L\mathbf{q}_L + \mathbf{F}_R - \mathbf{F}_L = 0,$$

and the RH condition across S_α^* becomes

$$(69) \quad S_\alpha(\mathbf{q}_\alpha^* - \mathbf{q}_\alpha) = \mathbf{F}_\alpha^* - \mathbf{F}_\alpha$$

Substituting (59) and (69) into (68) gives

$$(70) \quad |\mathbf{B}_{\text{HLL}} \cdot \mathbf{n}| \left(\frac{\mathbf{q}_R^{**}}{\sqrt{\rho_R^{**}}} + \frac{\mathbf{q}_L^{**}}{\sqrt{\rho_L^{**}}} \right) + \mathbf{F}_R^* - \mathbf{F}_L^* - S_R^* \mathbf{q}_R^* + S_L^* \mathbf{q}_L^* = 0.$$

Applying (70) to $\rho\mathbf{u}$ and using (67) and $\mathbf{u}_L^{**} = \mathbf{u}_R^{**}$ give

$$|\mathbf{B}_{\text{HLL}} \cdot \mathbf{n}| \left(\sqrt{\rho_R^*} + \sqrt{\rho_L^*} \right) \mathbf{u}_\alpha^{**} \\ + \left[(\mathbf{u} \cdot \mathbf{n})\rho\mathbf{u} + p_{\text{tot}}\mathbf{n} - (\mathbf{B} \cdot \mathbf{n})\mathbf{B} \right]_\alpha^* - \left[(\mathbf{u} \cdot \mathbf{n})\rho\mathbf{u} + p_{\text{tot}}\mathbf{n} - (\mathbf{B} \cdot \mathbf{n})\mathbf{B} \right]_\alpha^* - S_R^*(\rho\mathbf{u})_R^* + S_L^*(\rho\mathbf{u})_L^* = 0,$$

which, with (56)–(59), implies

$$(71) \quad \mathbf{u}_\alpha^{**} = \frac{\sqrt{\rho_L^*} \mathbf{u}_L^* + \sqrt{\rho_R^*} \mathbf{u}_R^* + \text{sign}(\mathbf{B}_{\text{HLL}} \cdot \mathbf{n})(\mathbf{B}_R^* - \mathbf{B}_L^*)}{\sqrt{\rho_L^*} + \sqrt{\rho_R^*}}.$$

Applying (70) to \mathbf{B} and using $\mathbf{B}_L^{**} = \mathbf{B}_R^{**}$ give

$$|\mathbf{B}_{\text{HLL}} \cdot \mathbf{n}| \left(\frac{1}{\sqrt{\rho_R^*}} + \frac{1}{\sqrt{\rho_L^*}} \right) \mathbf{B}_\alpha^{**} + [(\mathbf{u} \cdot \mathbf{n})\mathbf{B} - (\mathbf{B} \cdot \mathbf{n})\mathbf{u}]_R^* - [(\mathbf{u} \cdot \mathbf{n})\mathbf{B} - (\mathbf{B} \cdot \mathbf{n})\mathbf{u}]_L^* - S_R^* \mathbf{B}_R^* + S_L^* \mathbf{B}_L^* = 0,$$

which, with (56), (58) and (59) gives

$$(72) \quad \mathbf{B}_\alpha^{**} = \frac{\sqrt{\rho_R^*} \mathbf{B}_L^* + \sqrt{\rho_L^*} \mathbf{B}_R^* + \text{sign}(\mathbf{B}_{\text{HLL}} \cdot \mathbf{n}) \sqrt{\rho_L^* \rho_R^*} (\mathbf{u}_R^* - \mathbf{u}_L^*)}{\sqrt{\rho_L^*} + \sqrt{\rho_R^*}}.$$

The RH condition across S_α^* on \mathcal{E} gives

$$S_\alpha^* \mathcal{E}_\alpha^{**} - [(\mathcal{E} + p_{\text{tot}})(\mathbf{u} \cdot \mathbf{n}) - (\mathbf{u} \cdot \mathbf{B})(\mathbf{B} \cdot \mathbf{n})]_\alpha^{**} = S_\alpha^* \mathcal{E}_\alpha^* - [(\mathcal{E} + p_{\text{tot}})(\mathbf{u} \cdot \mathbf{n}) - (\mathbf{u} \cdot \mathbf{B})(\mathbf{B} \cdot \mathbf{n})]_\alpha^*,$$

which, with (56)–(59), gives

$$(73) \quad \mathcal{E}_\alpha^{**} = \mathcal{E}_\alpha^* \mp \sqrt{\rho_\alpha^*} (\mathbf{u}_\alpha^* \cdot \mathbf{B}_\alpha^* - \mathbf{u}_\alpha^{**} \cdot \mathbf{B}_\alpha^{**}) \text{sign}(\mathbf{B}_{\text{HLL}} \cdot \mathbf{n}),$$

where $-$ and $+$ correspond to $\alpha = \text{L}$ and R respectively.

Finally the intermediate states in the approximate solution are completely determined in (56)–(61), (64)–(67), (71)–(73).

REFERENCES

- [1] D. S. BALSARA, *Second-order-accurate schemes for magnetohydrodynamics with divergence-free reconstruction*, *Astrophys. J. Suppl. S.*, 151 (2004), p. 149.
- [2] D. S. BALSARA, *Divergence-free reconstruction of magnetic fields and WENO schemes for magnetohydrodynamics*, *J. Comput. Phys.*, 228 (2009), pp. 5040–5056.
- [3] D. S. BALSARA, *Multidimensional Riemann problem with self-similar internal structure. Part I—Application to hyperbolic conservation laws on structured meshes*, *J. Comput. Phys.*, 277 (2014), pp. 163–200.
- [4] D. S. BALSARA AND M. DUMBSER, *Multidimensional Riemann problem with self-similar internal structure. Part II—Application to hyperbolic conservation laws on unstructured meshes*, *J. Comput. Phys.*, 287 (2015), pp. 269–292.
- [5] D. S. BALSARA, C. MEYER, M. DUMBSER, H. DU, AND Z. XU, *Efficient implementation of ADER schemes for Euler and magnetohydrodynamical flows on structured meshes—speed comparisons with Runge-Kutta methods*, *J. Comput. Phys.*, 235 (2013), pp. 934–969.
- [6] D. S. BALSARA AND B. NKONGA, *Multidimensional Riemann problem with self-similar internal structure—Part III—A multidimensional analogue of the HLLI Riemann solver for conservative hyperbolic systems*, *J. Comput. Phys.*, 346 (2017), pp. 25–48.
- [7] D. S. BALSARA, T. RUMPF, M. DUMBSER, AND C.-D. MUNZ, *Efficient, high accuracy ADER-WENO schemes for hydrodynamics and divergence-free magnetohydrodynamics*, *J. Comput. Phys.*, 228 (2009), pp. 2480–2516.
- [8] D. S. BALSARA AND D. S. SPICER, *A staggered mesh algorithm using high order Godunov fluxes to ensure solenoidal magnetic fields in magnetohydrodynamic simulations*, *J. Comput. Phys.*, 149 (1999), pp. 270–292.
- [9] T. J. BARTH, *Numerical methods for gasdynamic systems on unstructured meshes*, in *An introduction to recent developments in theory and numerics for conservation laws*, Springer, 1999, pp. 195–285.
- [10] J. U. BRACKBILL AND D. C. BARNES, *The effect of nonzero $\nabla \cdot \mathbf{B}$ on the numerical solution of the magnetohydrodynamic equations*, *J. Comput. Phys.*, 35 (1980), pp. 426–430.
- [11] M. CASTRO, B. COSTA, AND W. S. DON, *High order weighted essentially non-oscillatory WENO-Z schemes for hyperbolic conservation laws*, *J. Comput. Phys.*, 230 (2011), pp. 1766–1792.
- [12] L. CHACÓN, *A non-staggered, conservative, finite-volume scheme for 3D implicit extended magnetohydrodynamics in curvilinear geometries*, *Comput. Phys. Commun.*, 163 (2004), pp. 143–171.
- [13] A. CHRISTLIEB, W. GUO, AND Y. JIANG, *Kernel based high order “explicit” A-stable scheme for nonlinear degenerate advection-diffusion equations*, arXiv preprint, arXiv:1707.09294, (2017).
- [14] A. J. CHRISTLIEB, X. FENG, D. C. SEAL, AND Q. TANG, *A high-order positivity-preserving single-stage single-step method for the ideal magnetohydrodynamic equations*, *J. Comput. Phys.*, 316 (2016), pp. 218–242.
- [15] A. J. CHRISTLIEB, Y. LIU, Q. TANG, AND Z. XU, *High order parametrized maximum-principle-preserving and positivity-preserving WENO schemes on unstructured meshes*, *J. Comput. Phys.*, 281 (2015), pp. 334–351.

- [16] A. J. CHRISTLIEB, Y. LIU, Q. TANG, AND Z. XU, *Positivity-preserving finite difference weighted ENO schemes with constrained transport for ideal magnetohydrodynamic equations*, SIAM J. Sci. Comput., 37 (2015), pp. A1825–A1845.
- [17] A. J. CHRISTLIEB, J. A. ROSSMANITH, AND Q. TANG, *Finite difference weighted essentially non-oscillatory schemes with constrained transport for ideal magnetohydrodynamics*, J. Comput. Phys., 268 (2014), pp. 302–325.
- [18] W. DAI AND P. R. WOODWARD, *On the divergence-free condition and conservation laws in numerical simulations for supersonic magnetohydrodynamical flows*, Astrophys. J., 494 (1998), p. 317.
- [19] W. DAI AND P. R. WOODWARD, *A simple finite difference scheme for multidimensional magnetohydrodynamical equations*, J. Comput. Phys., 142 (1998), pp. 331–369.
- [20] H. DE STERCK, *Numerical simulation and analysis of magnetically dominated MHD bow shock flows with applications in space physics*, PhD thesis, Katholieke University Leuven, 1999.
- [21] H. DE STERCK, A. CSIK, D. V. ABEELE, S. POEDTS, AND H. DECONINCK, *Stationary two-dimensional magnetohydrodynamic flows with shocks: characteristic analysis and grid convergence study*, J. Comput. Phys., 166 (2001), pp. 28–62.
- [22] A. DEDNER, F. KEMM, D. KRÖNER, C.-D. MUNZ, T. SCHNITZER, AND M. WESENBERG, *Hyperbolic divergence cleaning for the MHD equations*, J. Comput. Phys., 175 (2002), pp. 645–673.
- [23] W. D. D’HAESELEER, W. N. G. HITCHON, J. D. CALLEN, AND J. L. SHOHEET, *Toroidal Flux Coordinates*, Springer Berlin Heidelberg, Berlin, Heidelberg, 1991, pp. 116–155.
- [24] C. R. EVANS AND J. F. HAWLEY, *Simulation of magnetohydrodynamic flows – a constrained transport method*, Astrophys. J., 332 (1988), pp. 659–677.
- [25] M. FEY AND M. TORRILHON, *A constrained transport upwind scheme for divergence-free advection*, in *Hyperbolic problems: theory, numerics, applications*, Springer, Berlin, 2003, pp. 529–538.
- [26] T. A. GARDINER AND J. M. STONE, *An unsplit godunov method for ideal mhd via constrained transport*, Journal of Computational Physics, 205 (2005), pp. 509–539.
- [27] S. V. GOLOVIN, *Natural curvilinear coordinates for ideal MHD equations. Non-stationary flows with constant total pressure*, Physics Letters A, 375 (2011), pp. 283 – 290.
- [28] T. I. GOMBOSI, K. G. POWELL, AND D. L. DE ZEEUW, *Axisymmetric modeling of cometary mass loading on an adaptively refined grid: MHD results*, J. Geophys. Res.–Space, 99 (1994), pp. 21525–21539.
- [29] K. F. GURSKI, *An HLLC-type approximate Riemann solver for ideal magnetohydrodynamics*, SIAM J. Sci. Comput., 25 (2004), pp. 2165–2187.
- [30] A. HARTEN, P. D. LAX, AND B. VAN LEER, *On upstream differencing and Godunov-type schemes for hyperbolic conservation laws*, SIAM Rev., 25 (1983), pp. 35–61.
- [31] C. HELZEL, J. A. ROSSMANITH, AND B. TAETZ, *An unstaggered constrained transport method for the 3D ideal magnetohydrodynamic equations*, J. Comput. Phys., 230 (2011), pp. 3803–3829.
- [32] C. HELZEL, J. A. ROSSMANITH, AND B. TAETZ, *A high-order unstaggered constrained-transport method for the three-dimensional ideal magnetohydrodynamic equations based on the method of lines*, SIAM J. Sci. Comput., 35 (2013), pp. A623–A651.
- [33] W. D. HENSHAW, *A high-order accurate parallel solver for Maxwell’s equations on overlapping grids*, SIAM J. Sci. Comput., 28 (2006), pp. 1730–1765.
- [34] W. D. HENSHAW AND D. W. SCHWENDEMAN, *Moving overlapping grids with adaptive mesh refinement for high-speed reactive and non-reactive flow*, J. Comput. Phys., 216 (2006), pp. 744–779.
- [35] L. IVAN, *Development of high-order CENO finite-volume schemes with block-based adaptive mesh refinement*, PhD thesis, University of Toronto, 2011.
- [36] L. IVAN, H. D. STERCK, A. SUSANTO, AND C. GROTH, *High-order central ENO finite-volume scheme for hyperbolic conservation laws on three-dimensional cubed-sphere grids*, J. Comput. Phys., 282 (2015), pp. 157–182.
- [37] A. JEFFREY AND T. TANIUTI, *Non-linear wave propagation*, Mathematics in Science and Engineering, New York: Academic Press, 1964, 1 (1964).
- [38] G.-S. JIANG AND D. PENG, *Weighted ENO schemes for Hamilton–Jacobi equations*, SIAM J. Sci. Comput., 21 (2000), pp. 2126–2143.
- [39] G.-S. JIANG AND C.-W. SHU, *Efficient implementation of weighted ENO schemes*, J. Comput. Phys., 126 (1996), pp. 202–228.
- [40] G.-S. JIANG AND C.-C. WU, *A high-order WENO finite difference scheme for the equations of ideal magnetohydrodynamics*, J. Comput. Phys., 150 (1999), pp. 561–594.
- [41] Y. JIANG, C.-W. SHU, AND M. ZHANG, *An alternative formulation of finite difference weighted ENO schemes with Lax–Wendroff time discretization for conservation laws*, SIAM J. Sci. Comput., 35 (2013), pp. A1137–A1160.
- [42] Y. JIANG, C.-W. SHU, AND M. ZHANG, *Free-stream preserving finite difference schemes on curvilinear meshes*, Methods Appl. Anal., 21 (2014), pp. 1–30.
- [43] F. LI, L. XU, AND S. YAKOVLEV, *Central discontinuous Galerkin methods for ideal MHD equations with the exactly divergence-free magnetic field*, J. Comput. Phys., 230 (2011), pp. 4828–4847.
- [44] S. LI, *An HLLC Riemann solver for magneto-hydrodynamics*, J. Comput. Phys., 203 (2005), pp. 344–357.
- [45] P. LONDRILLO AND L. D. ZANNA, *High-order upwind schemes for multidimensional magnetohydrodynamics*, The Astrophysical Journal, 530 (2000), p. 508.
- [46] T. MIYOSHI AND K. KUSANO, *A multi-state HLL approximate Riemann solver for ideal magnetohydrodynamics*, J. Comput. Phys., 208 (2005), pp. 315–344.
- [47] H. NISHIDA AND T. NONOMURA, *ADI-SGS scheme on ideal magnetohydrodynamics*, J. Comput. Phys., 228 (2009), pp. 3182–3188.
- [48] T. NONOMURA, N. IIZUKA, AND K. FUJII, *Freestream and vortex preservation properties of high-order WENO and WCNS on curvilinear grids*, Comput. Fl., 39 (2010), pp. 197–214.
- [49] M. ROSENBLUTH AND M. BUSSAC, *MHD stability of spheromak*, Nucl. Fusion, 19 (1979), p. 489.
- [50] J. A. ROSSMANITH, *An unstaggered, high-resolution constrained transport method for magnetohydrodynamic flows*, SIAM

- J. Sci. Comput., 28 (2006), pp. 1766–1797.
- [51] D. C. SEAL, Q. TANG, Z. XU, AND A. J. CHRISTLIEB, *An explicit high-order single-stage single-step positivity-preserving finite difference WENO method for the compressible Euler equations*, J. Sci. Comput., (2015), pp. 1–20.
 - [52] Y. SHEN, G. ZHA, AND M. A. HUERTA, *E-CUSP scheme for the equations of ideal magnetohydrodynamics with high order WENO scheme*, J. Comput. Phys., 231 (2012), pp. 6233–6247.
 - [53] C.-W. SHU, *High order weighted essentially nonoscillatory schemes for convection dominated problems*, SIAM Rev., 51 (2009), pp. 82–126.
 - [54] C.-W. SHU AND S. OSHER, *Efficient implementation of essentially non-oscillatory shock-capturing schemes*, J. Comput. Phys., 77 (1988), pp. 439–471.
 - [55] A. SUSANTO, L. IVAN, H. D. STERCK, AND C. GROTH, *High-order central ENO finite-volume scheme for ideal MHD*, J. Comput. Phys., 250 (2013), pp. 141–164.
 - [56] K. TAKAHASHI AND S. YAMADA, *Regular and non-regular solutions of the Riemann problem in ideal magnetohydrodynamics*, J. Plasma Phys., 79 (2013), pp. 335–356.
 - [57] S. TAN AND C.-W. SHU, *Inverse Lax-Wendroff procedure for numerical boundary conditions of conservation laws*, J. Comput. Phys., 229 (2010), pp. 8144–8166.
 - [58] E. F. TORO, M. SPRUCE, AND W. SPEARES, *Restoration of the contact surface in the HLL-Riemann solver*, Shock Waves, 4 (1994), pp. 25–34.
 - [59] G. TÓTH, *The $\nabla \cdot B = 0$ constraint in shock-capturing magnetohydrodynamics codes*, J. Comput. Phys., 161 (2000), pp. 605–652.
 - [60] M. R. VISBAL AND D. V. GAITONDE, *On the use of higher-order finite-difference schemes on curvilinear and deforming meshes*, J. Comput. Phys., 181 (2002), pp. 155–185.
 - [61] A. L. ZACHARY, A. MALAGOLI, AND P. COLELLA, *A higher-order Godunov method for multidimensional ideal magnetohydrodynamics*, SIAM J. Sci. Comput., 15 (1994), pp. 263–284.